



Near-wall characteristics of wall-normal jets generated by an annular dielectric-barrier-discharge plasma actuator

Bal Krishan Mishra , Archana Gupta , and P. K. Panigrahi *

Department of Mechanical Engineering, Indian Institute of Technology Kanpur, Kanpur, Uttar Pradesh 208016, India



(Received 2 November 2021; accepted 18 March 2022; published 31 March 2022)

A dielectric-barrier-discharge plasma actuator with annular shape electrode geometry has been studied for evaluating the effectiveness in flow control applications. The flow field is investigated using time-resolved particle-image-velocimetry measurements and light-sheet flow visualization. The characterization of the actuator is carried out for both continuous- and burst-mode actuation. The Reynolds number, Re , of flow generated by the actuator is a function of actuation amplitude, ϕ_{pp} , and burst frequency, f_b , of the actuation signal, which governs the acceleration, development, and vortical structures of the wall-normal jet generated by the actuator. The maximum velocity generated by the actuator in continuous-mode actuation is higher than that of the burst-mode actuation. The velocity of the wall-normal jet increases in the wall-normal direction to a maximum value, v_{max} , followed by a gradual decay for both modes of actuation. The decay rate of v_{max} is a function of actuation mode due to the difference in nature of the vortex structure evolution and interaction. The overall flow field generated by the actuator can be divided into four zones: (i) entrainment zone, (ii) recirculation zone, (iii) developing zone, and (iv) self-similar zone. Three different types of vortices dominate the induced flow, i.e., (i) starting vortex or periodic vortex generated due to impulsive action, (ii) shear layer vortex formed due to roll-up of the shear layer, and (iii) recirculation vortex ring created due to deflection of the approaching wall boundary layer. The self-similar velocity profile of the wall-normal jet generated by the actuator is akin to that of a free jet. The wall-normal jet generated by continuous-mode actuation shows low-frequency ($f < 100$ Hz) vortical structures. In the burst mode, fluctuations are locked in with burst frequency for $f_b < 200$ Hz. For a higher value of burst frequency ($f_b > 200$ Hz), the effect is confined to the neighborhood of the exposed electrode, and flow field behavior approaches that of continuous-mode actuation.

DOI: [10.1103/PhysRevFluids.7.033702](https://doi.org/10.1103/PhysRevFluids.7.033702)

I. INTRODUCTION

The dielectric-barrier-discharge (DBD) plasma actuator is a potential alternative to common flow control devices such as discrete roughness elements, vortex generators, synthetic jets, gurney flaps, suction and blowing devices, etc., due to its several advantages, i.e., simple design, no moving parts, light weight, fully electronic, and low power consumption. Over the years, significant progress has been made in the development of DBD plasma actuators for flow control applications. The mechanism behind flow control provided by the DBD plasma actuator is based on interaction of main flow with the flow field generated by the actuator due to electrohydrodynamic body force. The structure of the flow field generated by the actuator can be controlled by introducing suitable geometric changes in the actuator design. Therefore, several designs of DBD plasma actuators have

*panig@iitk.ac.in

been proposed in the literature, offering unique advantages. Different types of flow field generated by the respective actuator design offer new opportunities for flow control [1–4]. The common profiles of exposed electrode edge are (a) straight line, (b) arc, (c) pulse, (d) comb/finger, (e) triangular, and (f) sawtooth. The DBD plasma actuator with a linear shape exposed electrode called the standard DBD plasma actuator generates a mean flow similar to a wall jet. The DBD plasma actuator with circular or annular shape electrode geometry called the “annular plasma synthetic jet actuator” (A-PSJA) generates a wall-normal jet by the interactions of counter-tangential jets. The counter-tangential jets can also be generated using contour electrode arrangement of linear shape exposed electrodes called the “linear plasma synthetic jet actuator” (L-PSJA) [5]. The A-PSJA can also be modified to act as a suction device by inverting the electrode arrangement to generate flow in the reverse direction [6].

The DBD plasma actuator with a circular electrode geometry was initially referred to as the “plasma synthetic jet actuator” (PSJA) by Santhanakrishnan and Jacob [6]. Later, in order to distinguish between the wall-normal jet created by the circular shape electrode and counterexposed electrode arrangement, they adopted the terminology “A-PSJA” for the circular shape and “L-PSJA” for linear shape counterexposed electrode. Some investigators have also termed it the “annular DBD plasma actuator” (see Humble *et al.* [7]; Neretti *et al.* [8]) or “ring-type plasma actuator” (see Choi and Kim [9]). In the literature, the terminology “PSJA” is also widely used for other configurations of plasma actuators known as the “SparkJet” actuator developed by Grossman *et al.* [10] and its other variants (see Cybyk *et al.* [11]; Ko *et al.* [12]; Wang *et al.* [13]; Zong and Kotsonis [14]; Huang *et al.* [15]). The working principle of the SparkJet actuator is different from that of the DBD plasma actuator. It consists of a small chamber with embedded electrodes and a discharge orifice. High chamber pressure is generated by rapidly heating the gas inside the cavity using an electrical discharge. The SparkJet is suitable for the control of high-speed flow [10,14]. The common feature between the conventional synthetic jet actuator, PSJA (SparkJet), and DBD-based PSJA (A-PSJA and L-PSJA) is that all are zero-net-mass-flux (ZNMF) devices. In this investigation, we have used the terminology “annular DBD plasma synthetic jet actuator” (A-DBD-PSJA) or “annular DBD plasma actuator” for A-PSJA and “linear DBD plasma synthetic jet actuator” (L-DBD-PSJA) for L-PSJA.

The wall-normal jet generated by A-DBD-PSJA is three-dimensional in nature, contrary to the nearly two-dimensional wall-normal jet generated by L-DBD-PSJA. A-DBD-PSJA affects the global flow field in contrast to the L-DBD-PSJA, which primarily affects the near-wall region [16]. Santhanakrishnan and his co-investigators investigated the flow field behavior of A-DBD-PSJA and its linear equivalent (L-DBD-PSJA) using experimental and numerical tools [5,6,17–19]. They carried out 2D particle-image-velocimetry (PIV) experiments to characterize the flow field induced by the A-DBD-PSJA. In their experiments, they operated the actuator in both continuous mode and burst mode at burst frequency f_b equal to 1, 10, and 100 Hz with a duty cycle $\alpha = 50\%$. They observed no unsteadiness in the flow field at $f_b = 100$ Hz and concluded that flow closely resembles the continuous-mode operation (i.e., steady flow) at $f_b = 100$ Hz. They simulated the behavior of L-DBD-PSJA using the body force model of Suzen *et al.* [20] and compared the simulation results with their experimental measurements. Liu *et al.* [21] applied the phenomenological body force formulation proposed by Shyy *et al.* [22] in the FLUENT platform to simulate the flow field behavior in both continuous and burst mode of actuation. They observed that the mean flow fields in both of the actuation modes are similar, having similarity with the plane jet and conventional synthetic jet. Ibrahim and Skote [23] used a modified form of the body force model proposed by Suzen *et al.* [20] that includes a time-varying boundary condition to account for the drift and diffusion in the electric field, and surface charge density in the COMSOL platform. They observed that the modified model predicts the centerline velocity more accurately.

Neretti *et al.* [8] investigated the effect of annulus diameter d_e on the performance of A-DBD-PSJA. They observed that the value of annulus diameter $d_e = 42$ mm provides the highest actuator efficiency, where the actuator efficiency is defined as the ratio of mechanical power to electrical power. The geometric dimension/size of the A-DBD-PSJA plays a significant role in the flow

induced by the actuator. A small dimension does not allow the formation of a wall-normal jet due to the minimum space required for mass entrainment, acceleration, and flow turning. Humble *et al.* [7] demonstrated that a millimeter-scale ($d_e = 3$ mm) annular DBD plasma actuator generates the flow field in a direction opposite to the flow field generated by a centimeter-scale A-DBD-PSJA. The flow generated by these millimeter-scale annular shape actuators develops a pair of necklace vortices around the actuator without shedding hairpin vortices, which helps in cross-flow instability control over a swept wing [9].

Segawa *et al.* [24] investigated the centimeter-scale annular DBD plasma actuator in burst mode at burst frequency $f_b = 0.5$ Hz with a duty cycle $\alpha = 5\%$. This combination of duty cycle and burst frequency only repeats the starting process in each burst. However, the annular DBD plasma actuator is expected to have more complex flow phenomena at higher values of burst frequencies. There is a critical frequency f_c below which differences in flow pattern between the continuous and burst mode operation are observed [25]. The wall-normal jet and vectored wall-normal jet generated by DBD plasma actuators were used by Borghi *et al.* [26] for flow control around a NACA0015 airfoil. They reported that the jet placed close to the leading edge provides the greatest stall recovery effect and the orientation of the wall-normal jet has no sensible effect on stall recovery. The burst mode operation was observed to be more effective than the continuous mode. The annular DBD plasma actuator placed around the coaxial jet has been observed to be successful in flow control by excitation of the outer shear layer [27].

The above literature review summarizes the complexities associated with the design of the annular DBD actuator and its importance for practical flow control applications. Most of the above literature has used low-speed PIV with maximum 15 Hz frequency. The present study is carried out using time-resolved (TR) PIV measurements at 1250 Hz fps leading to superior resolution of the temporal flow features. In addition, none of the above studies have focused on field of view concentrated on the near-wall region. Therefore, the primary objective of the present study is to explore the detailed flow features in the near-wall region of an annular DBD actuator. As a result, the present study is successful in demonstrating several flow features, i.e., the presence of a recirculation zone around the center of the annular actuator and standing wall-normal jet above it. Both continuous mode and burst mode of operation are studied. The parametric study on the effect of burst frequency and actuation voltage has been carried out. The average flow field behavior and the instantaneous flow structures presented in this study will be beneficial in the design and implementation of annular DBD actuators in several practical implementations.

II. METHODOLOGY

A. Experimental setup

Figure 1 shows the schematic of the experimental setup, including the instrumentation. The test facility involves two parts, one for the operation of the DBD plasma actuator, i.e., instrumentation for generating the DBD plasma, and the other one is for flow field measurements. The instrumentation used for the operation of the DBD plasma actuator comprises a high-frequency, high-voltage power amplifier, a function generator for controlling the input to the high-voltage power amplifier, an oscilloscope, and a high-voltage probe for the measurements of high-voltage signal applied to the actuator. The experimental arrangement for flow measurement includes a rectangular chamber made of plexiglass, seeding particle generator, a glass pitot tube, a micromanometer, and a TR-PIV system. More details about electrical instrumentation and the TR-PIV system can be found in our previous work [28–30]. All the experiments are carried out in quiescent air by placing the actuator inside the rectangular chamber (see Fig. 1). The volume of the chamber is $85 \times 36 \times 46.5$ cm³ (length \times width \times height), which is large enough in comparison to dimensions of the flow structures generated by the A-DBD-PSJA and the flow generated by the actuator can be assumed to be free from test chamber wall effects.

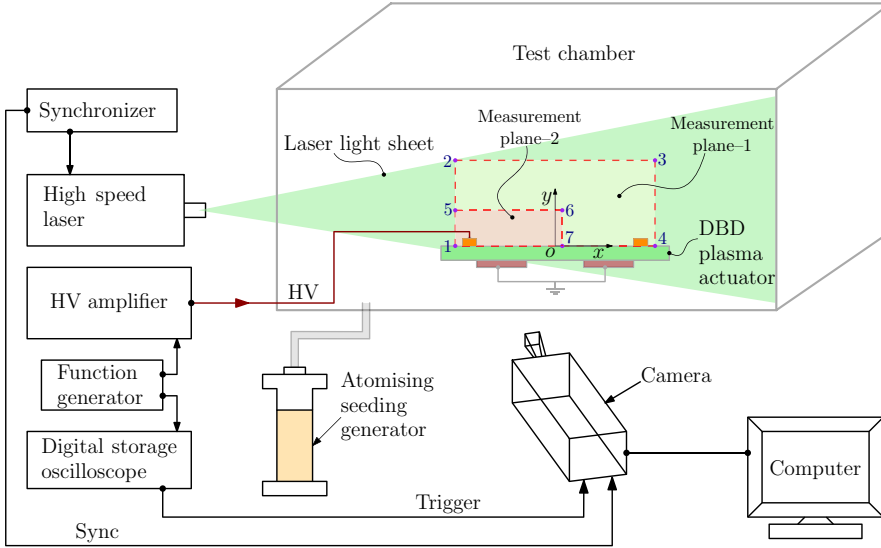


FIG. 1. Schematic of the experimental setup for the time-resolved PIV measurement. The measurement planes (1 and 2) are shown by the dotted rectangles (red in color). The measurement plane 2 shown by the boundary points 1-5-6-7 is used for near-wall measurements and measurement plane 1 having a larger field of view shown by the points 1-2-3-4 is used for the far-field measurements.

The seeding particles in the present study are generated by a commercial atomizer supplied by Oxford Lasers using dioctyl sebacate ($C_{26}H_{50}O_4$). The atomizer is operated by compressed air, which uses multiple Laskin nozzles to atomize the liquid. The aerosol particles generated by the atomizer range from $0.5\text{--}5\ \mu\text{m}$. Different sizes of seeding particles can be generated using the controls provided. There are four controls, each producing different size, i.e., from very fine to fine size particles. Hamdi *et al.* [31] and Gouriou *et al.* [32] investigated the effect of the high voltage on seeding particles used for PIV measurements. Hamdi *et al.* [31] compared the performance of different seeding for PIV measurement of electrohydrodynamic gas flow. Based on the results of tested particles, they observed that seeding particles like incense smoke, SiO_2 microballoons, and TiO_2 can be used for seeding the electrohydrodynamic gas flow. The effect of electrophoretic forces is also found to be negligible by Kim *et al.* [33]. Kriegseis [34] assumed the effect of the electric field to be negligible on seeding particles and used seeding particles generated from di-ethyl-hexyl-sebacate (DEHS) liquid for PIV measurements of flow induced by the DBD plasma actuator. In another study of flow induced by the plasma actuator, Zhang and Zong [35] used DEHS particles with a nominal diameter of μm generated by a commercial atomizer (Laskin-40) and estimated that the Stokes number S_k is of order 10^{-4} , where the stokes number S_k is given as

$$S_k = \frac{\rho_p d_p^2 u C_c}{18 \mu l}. \quad (1)$$

Here, ρ_p is the density of the particles, d_p is the seeding particle diameter, u is the maximum flow velocity, μ is the fluid viscosity, l is the characteristic length scale of the flow, and C_c is the slip correction factor. The condition $S_k < 0.1$ gives an adequate flow tracing accuracy with errors less than 1% [36]. Therefore, it can be assumed that tracer particles accurately follow the induced flow and effect of electrical charging is negligible.

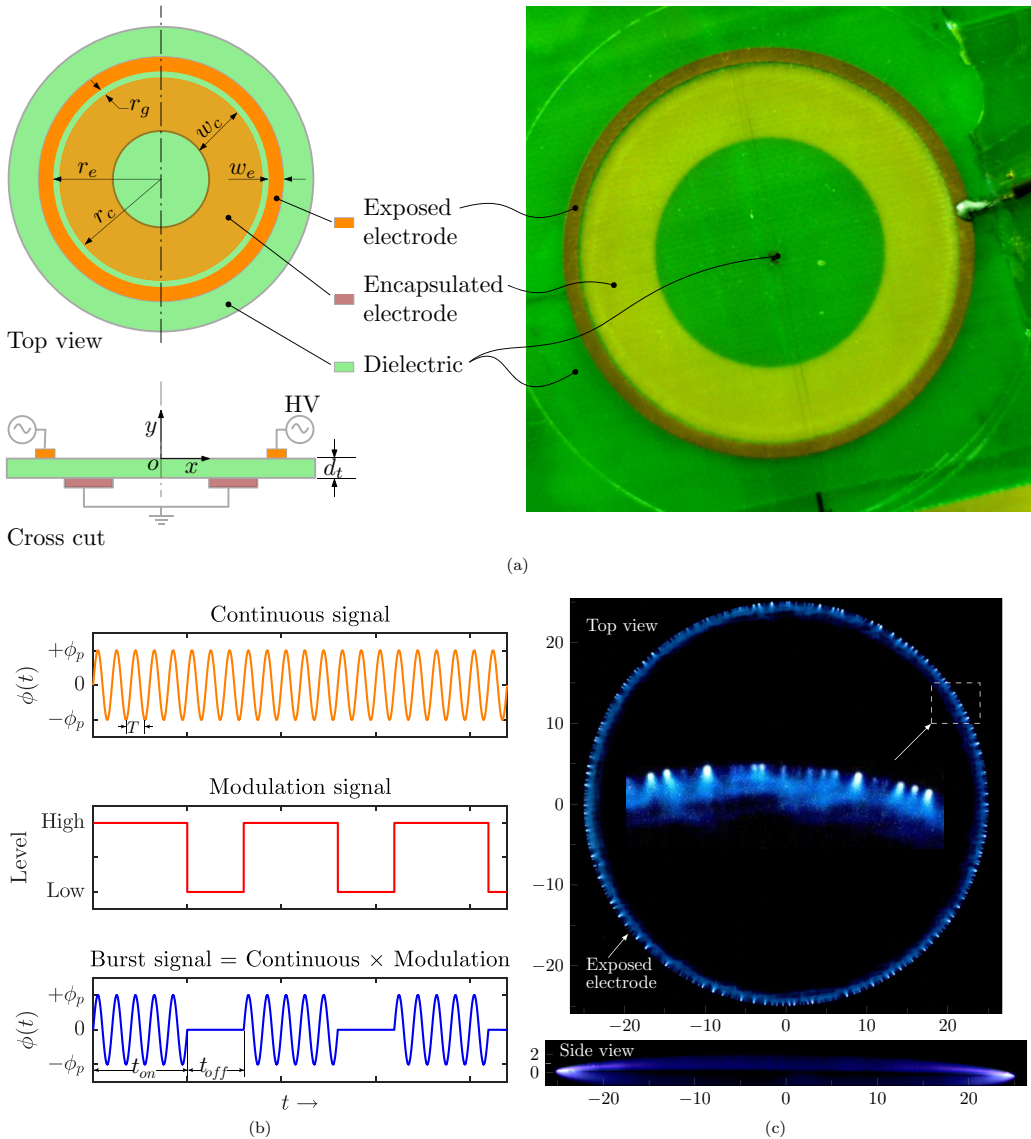


FIG. 2. (a) The schematic of an annular DBD plasma actuator, along with the photograph of the actuator fabricated for the present investigation, (b) representation of the actuation signals (continuous and burst), and (c) photograph of plasma discharge produced by the actuator (top view and side view). This plasma discharge image corresponds to the continuous mode of operation with $\phi_{pp} = 8.8$ kV and $f_{ac} = 8$ kHz, and unit of the axis values is in millimeters. The extra bright spots at the edge of the exposed electrode in top view image are microdischarge spikes (see multimedia view in the Supplemental Material [48]).

B. Actuator and actuation parameter

Figure 2(a) shows the schematic of an annular DBD plasma actuator along with the photograph of the actuator as viewed from the top. The DBD plasma actuator is manufactured using the printed circuit board (PCB) technology for high geometric precision. The PCB acts as a dielectric for the actuator, and it is made of flame retardant material, FR-4, having a dielectric constant of 4.7. The electrodes are etched in a circular shape on the top and bottom surface of the PCB using copper as

the material of electrodes. The dimensions of the actuator (see Fig. 2) are as follows: inner diameter of the exposed electrode, $d_e = 50$ mm; thickness of the dielectric, $d_l = 1$ mm; width of exposed electrode, $w_e = 2$ mm; width of covered electrode, $w_c = 10$ mm; and the electrode gap, $r_g = 0$ mm.

The actuator can be operated in continuous and burst modes using continuous and burst signals, respectively. The AC input signals applied to the actuator for both continuous mode and burst mode are shown in Fig. 2(b). The burst signal is a modulated continuous signal achieved by taking the product of the continuous signal and modulation signal. The actuation signal, $\phi(t)$, denotes the amplitude of signal which is periodic in time, t , with a time period of T and peak-to-peak amplitude of ϕ_{pp} ($-\phi_p$ to $+\phi_p$). The frequency of AC wave form is defined as $f_{ac} = 1/T$. The parameters of the burst signal are defined as follows: t_{on} is burst or ON time and t_{off} is idle or OFF time of the burst signal; burst period, $t_b = t_{on} + t_{off}$; burst frequency, $f_b = 1/t_b$; and duty cycle, $\alpha = t_{on}/t_b$. The exposed electrode is connected to the high-voltage source, and the encapsulated electrode is grounded.

Figure 2(c) shows the top view and side view of the DBD plasma flow generated by the actuator, respectively. It also reveals the fact that ionization takes place only near the exposed electrode and discharge of plasma extends up to a few millimeters toward the covered electrode. The top view images further display the presence of microdischarges distributed around the entire perimeter of the exposed electrode. These microdischarges randomly switch and change their location (see the multimedia view in the Supplemental Material [48]). The bright region of the plasma discharge visualized in the side view shows its transverse extent which is less than one millimeter. The microdischarge remains organized and separated by some angular distance. The plasma discharge structure is similar to that of the millimetric-size annular DBD plasma actuator investigated using a photomultiplier tube in more detail by Humble *et al.* [7].

C. Experimental procedure and parameters

The experiments were conducted in two separate stages. In the first stage, a large field of view (FOV) (measurement plane 1) is selected (see Fig. 1) which includes far-field as well as the near-wall region of the actuator. In the second stage, a smaller FOV (measurement plane 2) was selected to capture the near-wall region flow field details with a higher spatial resolution. The coordinate system chosen for the description of the flow field is fixed at the geometric center of the annulus as shown in Figs. 1 and 2(a). The small FOV includes only one half (left half) of the flow field about the central axis and extends up to a distance $y/d_e = 0.34$ in the wall-normal direction. The size of the large FOV is 1024×1094 pixels², which is equivalent to 64×68.5 mm² in real dimensions and thus has a spatial resolution of 1 pixel = 62.5 μ m. The size of the small FOV is 1280×720 pixels² which is equivalent to 31.4×17.6 mm² having a spatial resolution of 1 pixel = 24.5 μ m (approximately 2.55 times greater than of spatial resolution provided by the large-FOV measurements). However, the same increase in spatial resolution could not be maintained in PIV postprocessing due to constraints of particle density and frame rate. The spatial resolution of the PIV vector field is 1 mm and 0.784 mm for the large-FOV and small-FOV cases, respectively. The PIV images for both the large-FOV and small-FOV measurements were recorded at the same frame rate of 2500 frames per second.

The flow path lines can be experimentally obtained by providing multiple exposures of light for a single frame. In the present study, the flow visualization images were reconstructed by implementing the concept of multiple exposures in MATLAB using time-resolved images. We have used an ensemble of 15 sequential images acquired at 2500 fps and added them together to construct the flow visualization images. Thus, the effective frame rate for the flow visualization images reduces to 166.67 fps. For the correct phase reference, the camera trigger signal is synchronized with input to the high-voltage amplifier such that the first image of cine recording corresponds to start of the actuator. The same procedure is followed for the postprocessing of PIV images as mentioned in our previous work [30]. The accuracy of velocity measurements from TR-PIV measurement was verified by repeating a set of velocity measurements using a glass pitot tube and a micromanometer.

TABLE I. Details of the experimental conditions used in the present study. The frequency of actuation signal, $f_{ac} = 8$ kHz, is kept constant in all the experiments. The Reynolds numbers, $Re_d = v_{\max}d_e/\nu$ and $Re_{\delta_{1/2}} = v_{\max}\delta_{1/2}/\nu$, were calculated after postprocessing of PIV data.

| Continuous mode | | | | | | | | Burst mode ($\phi_{pp} = 8$ kV and $\alpha = 70\%$) | | | | | | |
|-----------------------|------|------|------|------|------|------|------|---|-----------------------|------|------|------|------|------|
| Case No.: | 1 | 2 | 3 | 4 | 5 | 6 | 7 | 8 | Case No.: | 9 | 10 | 11 | 12 | 13 |
| ϕ_{pp} (kV): | 7.4 | 7.6 | 7.8 | 8.0 | 8.2 | 8.6 | 8.8 | 9.8 | f_b (Hz): | 10 | 25 | 50 | 100 | 200 |
| Re_d : | 2620 | 2890 | 3144 | 3283 | 3550 | 4111 | 4368 | 5753 | Re_d : | 1978 | 1980 | 2078 | 2175 | 2180 |
| $Re_{\delta_{1/2}}$: | 312 | 452 | 531 | 514 | 511 | 591 | 572 | 758 | $Re_{\delta_{1/2}}$: | 407 | 459 | 427 | 396 | 397 |

The actuator is operated in both continuous mode and burst mode. In continuous mode, the value of actuation voltage, ϕ_{pp} , is selected as an operational variable by fixing the actuation frequency value, $f_{ac} = 8$ kHz. For the burst mode, the burst signal parameter f_b is chosen as an operational variable by fixing the duty cycle, $\alpha = 70\%$, and the parameters of the high-voltage AC signal at $\phi_{pp} = 8$ kV and $f_{ac} = 8$ kHz. The selection of f_b as a variable for the burst mode is carried out based on the nature of flow structures generated by a standard DBD plasma actuator in burst mode [25,37]. Detailed information on operating test conditions is provided in Table I.

The increase in applied input voltage results in a stronger ionization, increased plasma density, and greater electrohydrodynamic body force. Since the electrohydrodynamic body force $F_B \propto E$, where E is the strength of applied electric field, the increased magnitude of electrohydrodynamic body force induces a flow field with a greater velocity. Thus, investigating the effect of ϕ_{pp} serves the objective of studying the Reynolds number effect. The Reynolds number, Re , is estimated in two different manners using two separate length scales, (i) the Reynolds number based on diameter of annulus, $Re_d = v_{\max}d_e/\nu$, and (ii) the Reynolds number based on jet half-width, $Re_{\delta_{1/2}} = v_{\max}\delta_{1/2}/\nu$, where v_{\max} is the global maximum velocity, $\delta_{1/2}$ is the half-width of the wall-normal jet, and ν is the kinematic viscosity of the air. In the absence of any initial velocity, the values of Re are estimated after the postprocessing of experimental data. The values of $Re_{\delta_{1/2}}$ are estimated using the value of $\delta_{1/2}$ at the location of v_{\max} . The values of Re_d and $Re_{\delta_{1/2}}$ corresponding to each operating condition are provided in Table I. The values of Re_d and $Re_{\delta_{1/2}}$ show an increasing trend with increasing values of ϕ_{pp} . The distances are normalized by d_e and flow properties are either normalized by their respective local maximum or global maximum. The results from small-FOV (near-wall) measurements are presented first, and the results obtained from large-FOV (full-field) measurements are reported subsequently.

III. RESULTS AND DISCUSSION

A. Starting vortex and recirculation zone formation

Figure 3 shows the sequence of instantaneous visualization images in the near-wall region for continuous-mode actuation at excitation voltage, $\phi_{pp} = 8$ kV. The flow field is shown at one side of the annular geometry. Figure 3(a) shows that a starting vortex is created just after the activation of the actuator as a consequence of impulsive forcing in a manner similar to the starting vortex created by the standard DBD plasma actuator. The starting vortex travels radially inward toward the geometric center of the annular actuator at an angle of θ with simultaneous growth in size. The angle of travel, θ , is defined as the angle made by the line passing through the vortex core, which meets the dielectric surface at the edge of the exposed electrode [see Fig. 3(a)]. The angle θ increases with time while traveling toward the centerline of the annular actuator, which is unlike the constant value of $\theta \approx 31^\circ$ for the starting vortex created by the standard DBD plasma actuator [29,38]. In the later stage, the vortex starts convecting in the wall-normal direction away from the wall leading to rapid increase in the magnitude of angle θ . The transverse motion in the wall-normal direction leads to flow detachment from the wall surface resulting in the formation of a recirculation zone around

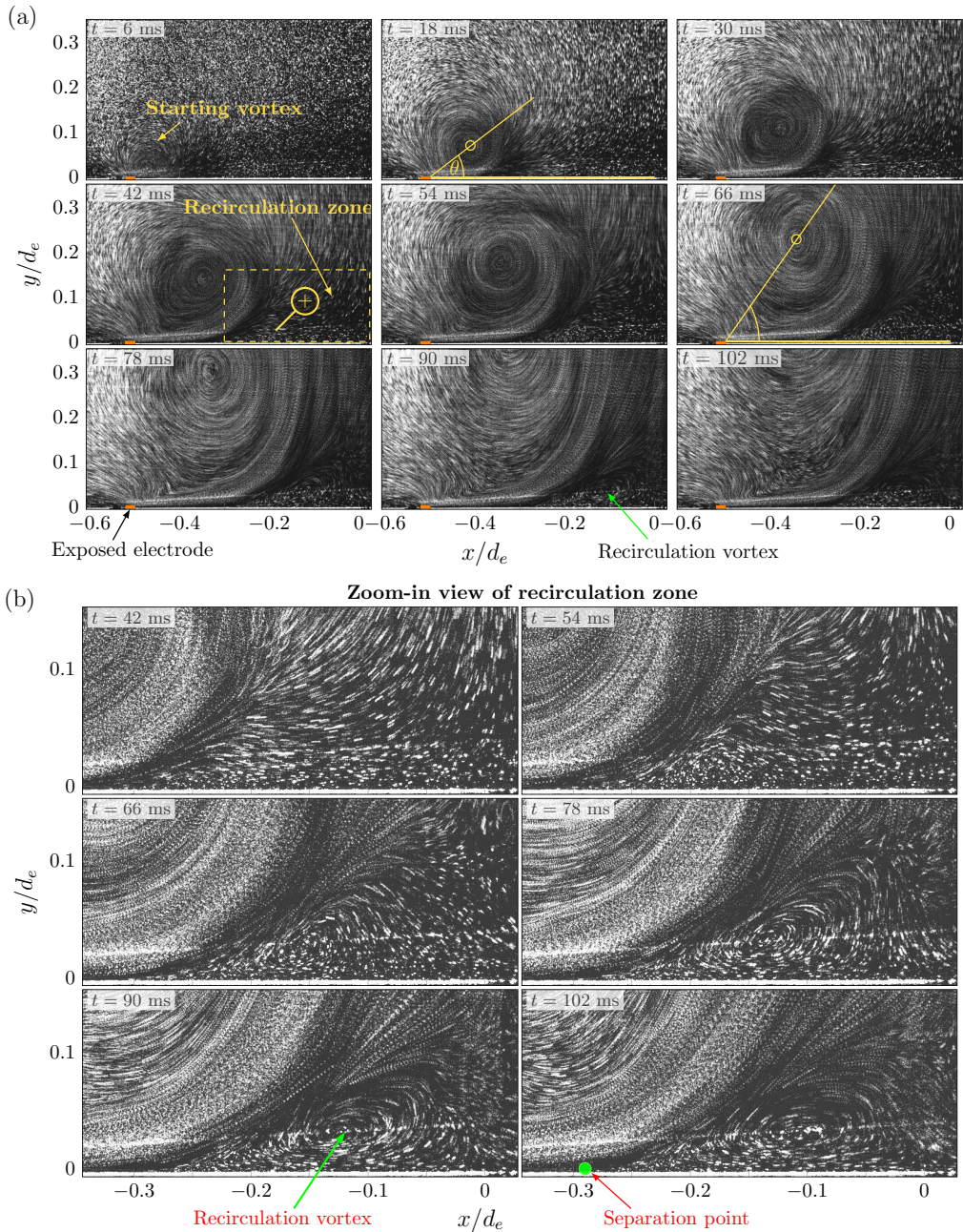


FIG. 3. (a) Instantaneous visualization images showing the development of starting vortex and formation of recirculation zone (flow is from left to right), where the recirculation zone is marked with a dotted rectangle, and (b) the zoom-in view of the recirculation zone. The time $t = 0$ refers to start of the actuator and the actuator is operating in continuous mode at $\phi_{pp} = 8$ kV and $f_{ac} = 8$ kHz (case 4). The multimedia video in the Supplemental Material [48] shows the behavior of starting vortex as a function of actuation voltage, ϕ_{pp} .

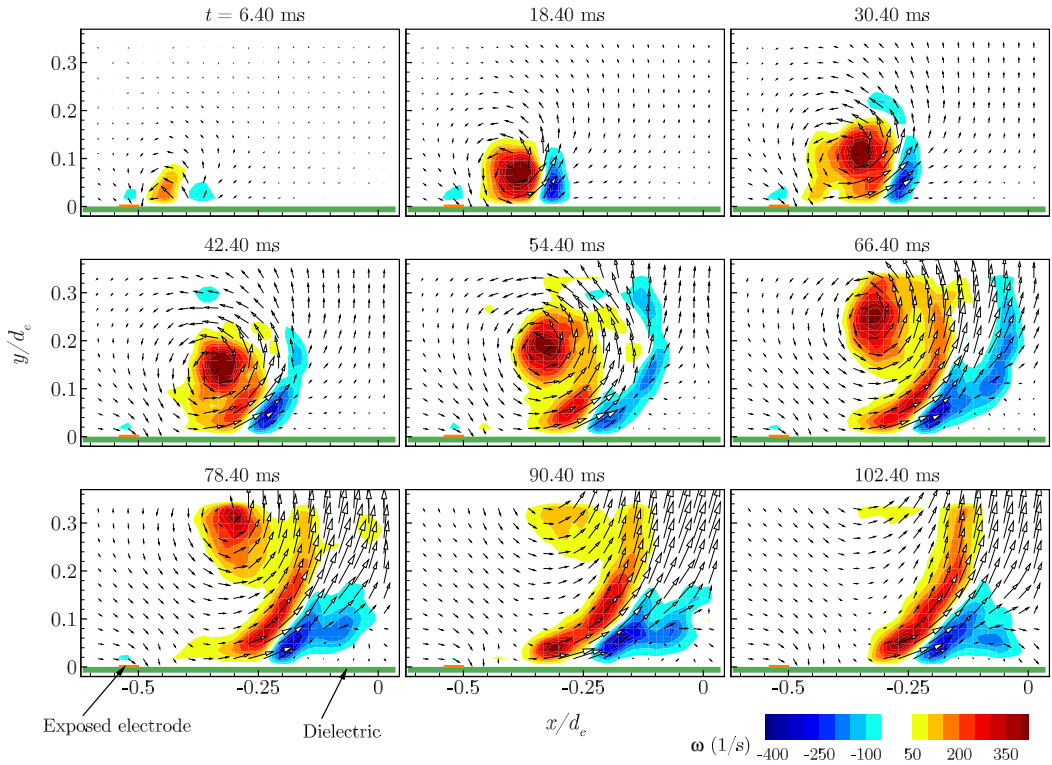


FIG. 4. Flow field of starting vortex development corresponding to flow visualization images shown in Fig. 3. The velocity vectors are superimposed on isocontours of vorticity. The color map level is the same for all time instants.

the origin. The level of actuation voltage, ϕ_{pp} , strongly influences the development of the starting vortex, and its effect can be seen in the multimedia movie provided for Fig. 3. The increasing value of ϕ_{pp} increases the induced velocity, and the starting vortex travels at a faster speed. The starting vortex convecting with a greater core velocity leads to a steady (more precisely, quasisteady) flow condition in a short interval of time in comparison to the lower values of actuation voltage, ϕ_{pp} .

Figure 3(b) shows an enlarged view [see the region bounded by dashed lines in Fig. 3(a)] of recirculation zone for the period starting from $t = 42$ to 102 ms. After the time instant of $t = 102$ ms, no remarkable change is observed in the behavior of the recirculation zone. The recirculation zone indicates the formation of a vortex ring around the centerline of the actuator. The midplane visualizations show that the vortex ring remains almost axisymmetric for low-excitation voltage ϕ_{pp} , i.e., for low Re. For a greater value of ϕ_{pp} , i.e., at higher Re, the vortex inside the recirculation zone randomly breaks down due to unsteadiness associated with higher Re. This behavior can be visualized at $\phi_{pp} = 9.8$ kV in multimedia movie for Fig. 3. The separation point is located near $x/d_e \approx 0.29$ which also moves closer to the annulus center with increasing Re.

Figure 4 presents the instantaneous velocity vector field corresponding to the instantaneous visualization images presented in Fig. 3(a). When the actuation is initiated, positive vorticity is created near the exposed electrode due to motion of the surrounding fluid. The surrounding fluid is set into motion because of momentum exchanged by the net motion of ions from the exposed electrode to the encapsulated electrode. Negative vorticity is created ahead of the positive vorticity region due to the viscous effects, and with the progress of time, the positive vorticity leads to formation of the starting vortex. The magnitude and size of both positive vorticity and negative

vorticity regions increase with time. The negative vorticity region is carried away by the outer periphery of the starting vortex in a manner such that the starting vortex tries to get wrapped by the negative vorticity (see at $t = 18.4$ ms to 66.4 ms). As the time progresses, the negative vorticity is detached from the starting vortex and remains attached to the wall surface with formation of a positive shear layer region around the center of the actuator. The time required for the formation of the steady shear layer region is of the order of milliseconds, which depends on the magnitude of induced flow velocity, i.e., actuation voltage level.

B. Steady and periodic flow behavior

In continuous-mode operation, the steady or quasisteady flow condition is attained after a short time of interval [$O(\text{ms})$] from the start of the actuation. On the other hand, burst-mode operation leads to the development of periodic shedding of vortices. Figure 5 shows the instantaneous flow visualization images of periodic flow generated by the burst mode actuation as a function of burst frequency ($f_b = 10$ Hz, 25 Hz, and 50 Hz). The periodic flow condition is confirmed by the inspection of visualization images for a long time interval. The flow visualization images are presented for five successive time instants in a nondimensional time frame. The instantaneous time t is normalized by the burst cycle time t_b , where $t = 0$ corresponds to the start of burst cycle. The time instant t/t_b for images are chosen according to its physical relevance with respect to one complete burst cycle. The physical relevance of selected t/t_b for a constant value of $\alpha = 70\%$ is as follows: (i) $t/t_b = 0$ represents the start of the burst cycle, (ii) $t/t_b = 0.35 = t_{\text{on}}/2$ corresponds to the middle of the burst duration, (iii) $t/t_b = 0.7 = t_{\text{on}}$ corresponds to the end of the burst duration, and (iv) $t/t_b = 1$ represents the end of the burst cycle. To show the repeatability of periodic flow structures, visualization results at the middle of burst length, $t/t_b = 0.35$, are compared with periodic flow structures obtained after completion of three consecutive burst cycles at $t/t_b = 3.35$. However, it is not possible to extract the images exactly at the specified time interval due to a combination of frame rate and burst period, t_b , effect. Therefore, the images are shown for the time instant closest to the specified time instant. The comparison of visualization images at $t/t_b = 0.35$ with the images after three burst cycle periods at $t/t_b = 3.35$ for all burst frequency cases ($f_b = 10$ Hz, 25 Hz, and 50 Hz) confirms the periodic nature of the induced flow.

Figure 5 reveals the formation of a large periodic vortex at a low value of burst frequency, $f_b = 10$ Hz, in comparison to a higher value of $f_b = 50$ Hz. This can be verified by comparing the visualization images at time instant of $t/t_b \approx 0.35$. The size of periodic vortices reduces further with increase in f_b , and at $f_b = 100$ Hz, the size of the vortices is very small. At $f_b = 200$ Hz, we could not trace any periodic vortices (see the multimedia for Fig. 5). The flow remains in quasiperiodic condition with minor changes and it can be noticed by comparing the results at $t/t_b \approx 0.35$ and 3.35 for each case. The rate of periodic vortex production increases with increasing f_b . A small time interval between the two consecutive periodic vortex shortens the distance between the vortices. The recirculation zone behavior is also strongly influenced by low values of burst frequency, $f_b = 10$ Hz and 25 Hz, and recirculation vortex ring formation occurs periodically (see the multimedia file).

Figure 6 shows the contours of vorticity with superimposed velocity vectors corresponding to the instantaneous visualization images shown in Fig. 5. At the start of the burst cycle $t/t_b \approx 0$, the remnant flow condition is not the same for all burst frequency cases which indicates that the initial condition for the start of a new burst cycle depends on the burst frequency. For a low value of $f_b = 10$ Hz, the remnant flow is sufficiently far away from the neighborhood of the exposed electrode. Therefore, the incipient flow due to the succeeding burst cycle is subjected to minor strain from the remnant flow. Consequently, the periodic vortex formed at low burst frequencies approximates the behavior of the starting vortex. The distance between the remnant fluid and the exposed electrode decreases with an increase in burst frequency. At burst frequency $f_b = 25$ and 50 Hz at time $t/t_b = 1$, the remnant fluid is present closer to the location of the exposed electrode in the form of remnant vortices. The remnant vortices interact with freshly shed vortices. The differences in periodic vortex generated at different burst frequencies can be attributed to the initial condition at the start of each

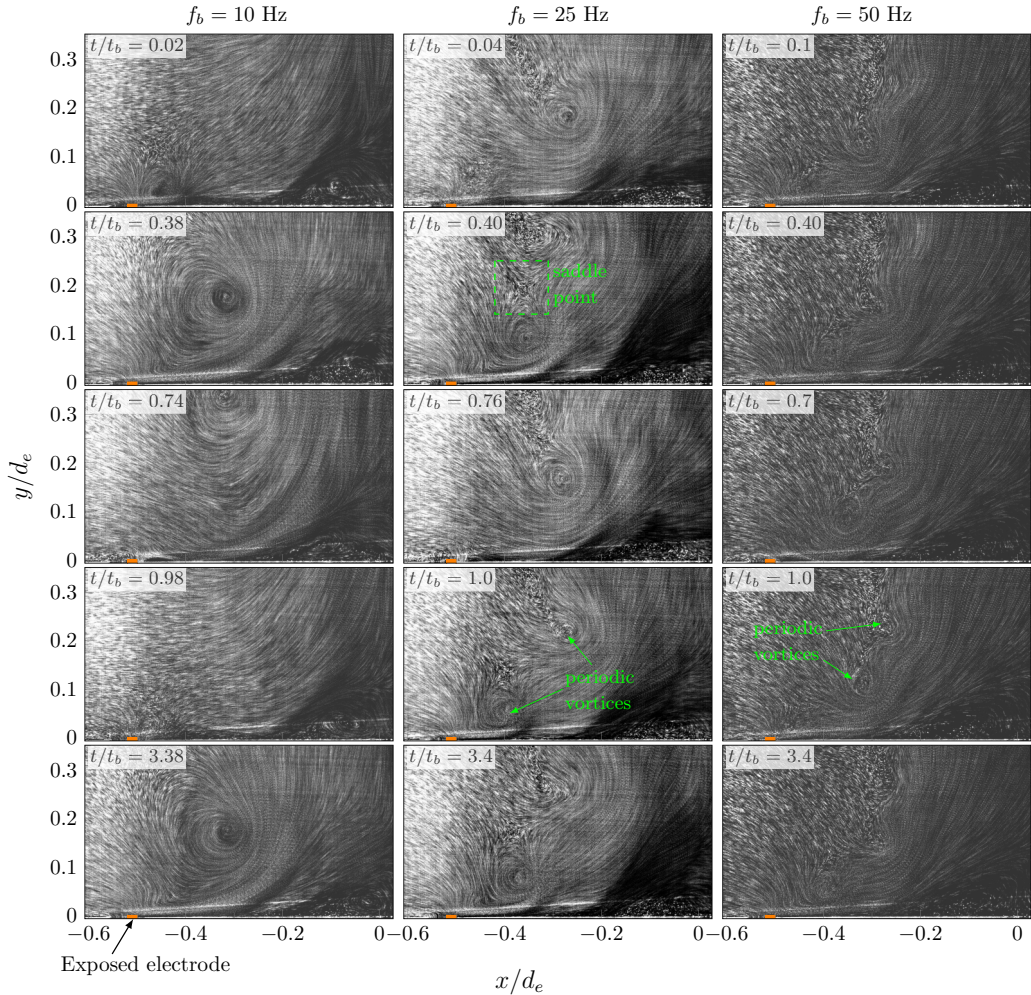


FIG. 5. Instantaneous visualization images showing the behavior of periodic vortices generated in burst-mode operation at $f_b = 10$ Hz (left column), 25 Hz (middle column), and 50 Hz (right column). The time interval increases from top to bottom and the time $t/t_b = 0$ refers to start of the burst signal. The multimedia view in the Supplemental Material [48] shows the flow structures in burst mode as a function of burst frequency, f_b .

burst cycle. By doubling the burst frequency, $f_b = 100$ Hz, the size of the periodic vortex becomes very small, and more periodic vortices are present in the remnant flow. With further increase in burst frequency to 200 Hz, the vortices cannot form due to a very short time period of impulse and larger influence of remnant flow condition.

Figure 7 shows the instantaneous flow visualization images of steady flow with increasing values of actuation voltage, ϕ_{pp} , in continuous-mode operation. The effect of ϕ_{pp} on actuator performance is a net increase in the magnitude of induced flow velocity. Thus, Fig. 7 also demonstrates the characteristic of flow as a function of increasing Reynolds number. The value of $Re_{\delta_{1/2}}$ corresponding to each value of ϕ_{pp} is presented in Table I. The separation point moves closer toward the origin, i.e., toward the geometric center of the annular actuator for increasing values of ϕ_{pp} . It is also observed that at higher value of Re , the initial radially inward parallel flow turns in the wall-normal direction at a larger turning angle. This behavior is attributed to a higher flow velocity induced at high voltage

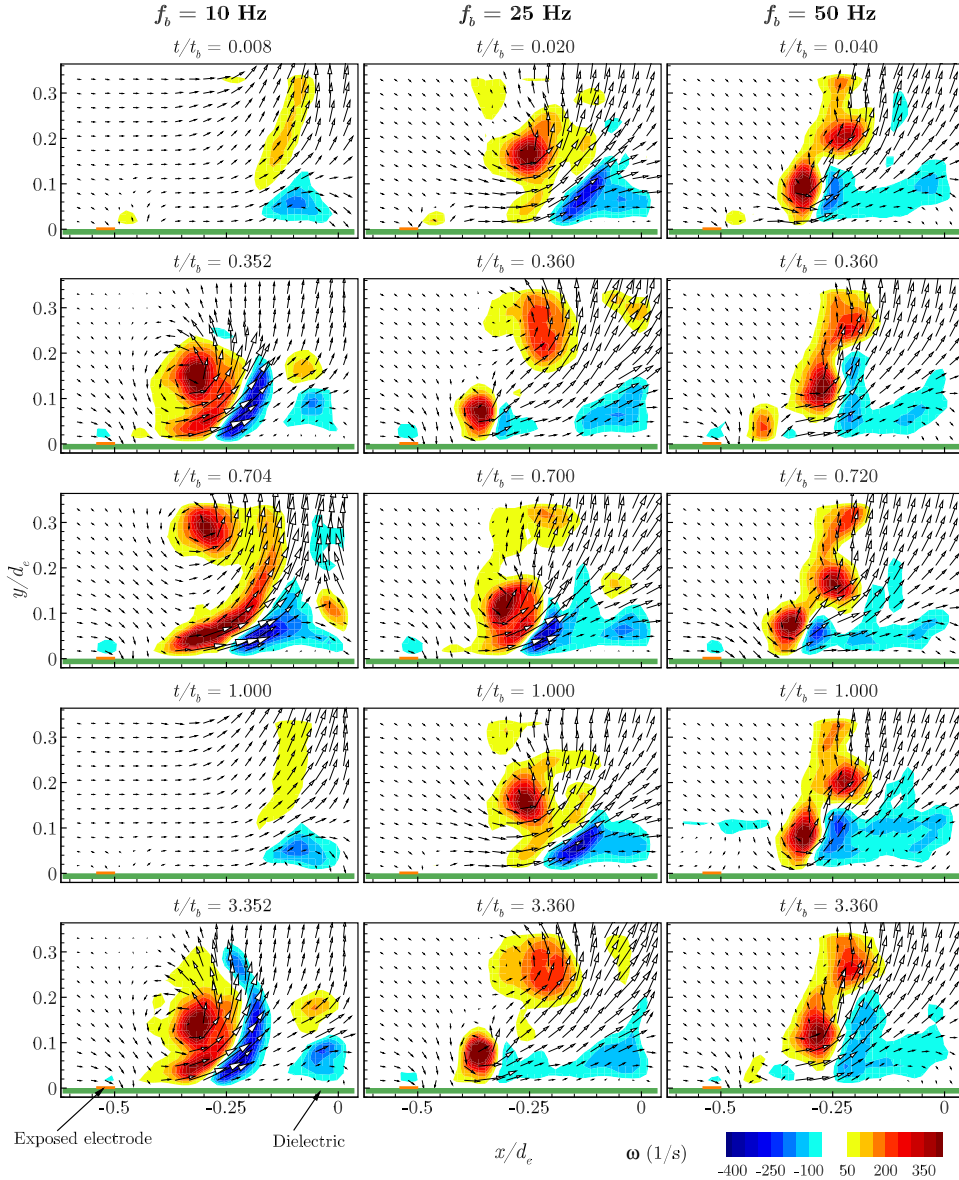


FIG. 6. Instantaneous flow field showing the behavior of periodic vortices generated by the actuator in burst-mode operation at $f_b = 10$ Hz (left column), 25 Hz (middle column), and 50 Hz (right column).

level, which causes delay in flow separation; i.e., the location of the separation point shifts farther from the exposed electrode toward the center of the actuator. The recirculation region shrinks as the separation point approaches the origin. At a higher value of ϕ_{pp} , the flow inside the recirculation zone becomes more dynamic in nature. The vortex inside the recirculation zone is momentarily generated, which subsequently breaks down leading to unsteadiness inside the recirculation zone.

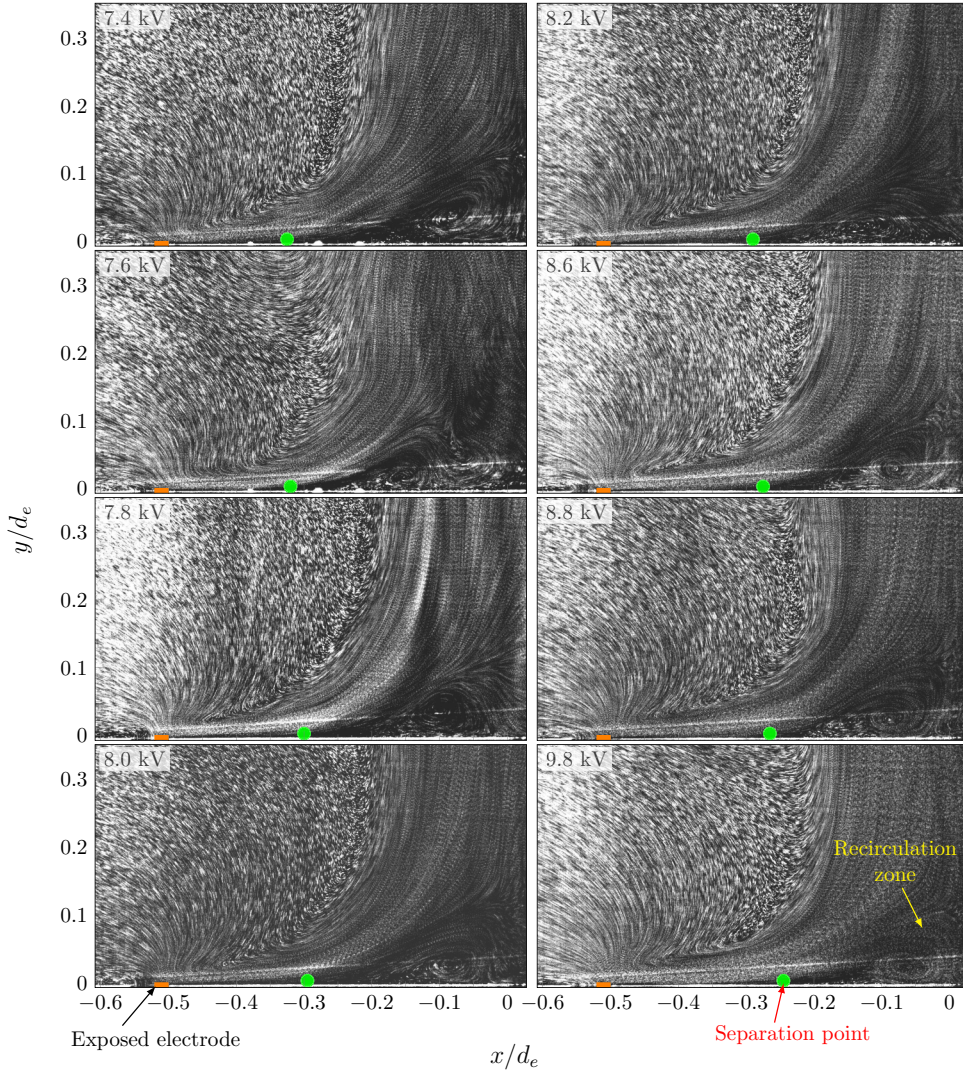


FIG. 7. Instantaneous visualization images as a function of actuation voltage, ϕ_{pp} , in continuous mode, demonstrating the effect of increasing Reynolds number, Re . Notice the recirculation zone is present at all actuation voltage levels (multimedia view in the Supplemental Material [48]).

C. Wall-normal jet behavior

Figure 8 shows the mean flow characteristics using isocontours of nondimensional vorticity, ω/ω_{\max} , and velocity vectors as a function of ϕ_{pp} and f_b for the continuous mode and burst mode of actuation, respectively. It may be noted that for the calculation of the mean flow field, only steady or periodic flow data have been used, and the initial starting vortex data are not included for averaging. The flow is initiated parallel to the actuator surface starting from the vicinity of the exposed electrode which travels radially inward and separates at an upstream location before the center of the actuator. The separated boundary layer generates a recirculation zone with a clockwise rotation toward the central axis. The velocity of induced flow increases with an increase in actuation voltage, ϕ_{pp} , for the continuous-mode actuation. The increase in velocity is attributed to higher magnitude of body force, $F_B = qE$, which is directly proportional to the strength of the applied electric field, E . At a

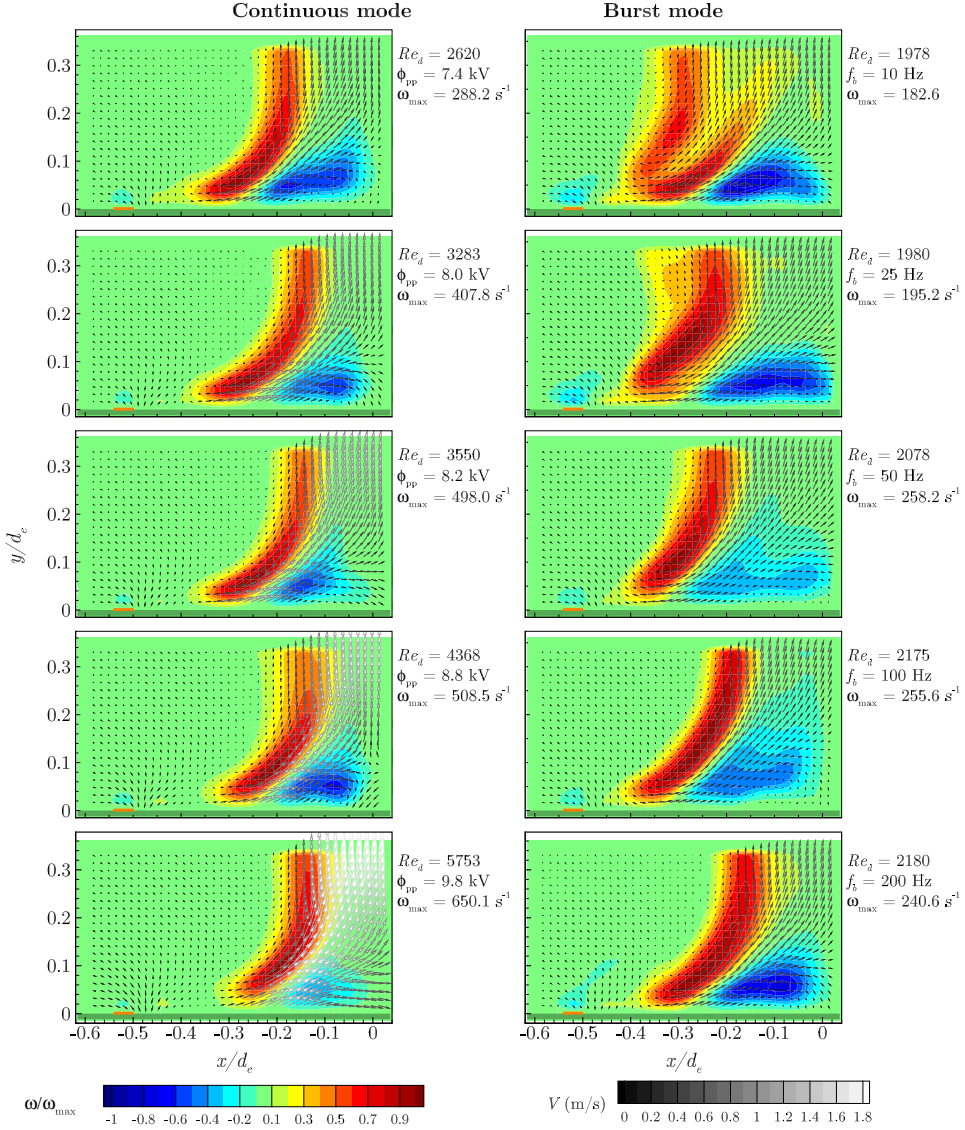


FIG. 8. Time-averaged flow field from near-wall measurements in continuous mode as a function of actuation voltage, ϕ_{pp} (left column), and in burst mode as a function of burst frequency, f_b (right column). Both ϕ_{pp} and f_b are increasing from top to bottom. The velocity vectors are superimposed on isocontours of vorticity, ω , normalized by its absolute maximum, ω_{\max} , which is mentioned in legend of respective plots. The magnitude of absolute velocity, $V = \sqrt{u^2 + v^2}$, is shown by the color of velocity vectors.

higher induced velocity, the fluid carries more momentum leading to a delay in separation. Both Reynolds number, Re , and maximum vorticity, ω_{\max} , increase with an increase in actuation voltage for the continuous-mode actuation case. The delay in separation also leads to a smaller recirculation bubble size at higher actuation voltage for continuous-mode actuation.

The overall mean flow behavior for the burst-mode actuation is similar to that of the continuous mode of actuation. However, the average velocity for the burst-mode actuation is lower than that of the continuous mode. As a result, the values of Reynolds number and maximum vorticity for

burst mode of actuation are lower than those of continuous mode. The separation occurs earlier for the burst mode compared to the continuous mode at the same actuation voltage. The separation point shifts toward the central axis with increase in burst frequency. Comparing the flow field at $f_b = 100$ Hz and 200 Hz with its continuous-mode counterpart at $\phi_{pp} = 8.0$ kV, Fig. 8 further reveals that with increasing values of f_b the flow behavior tends to approximate the flow topology of continuous mode. The positive shear region is wider for the low-frequency burst-mode actuation compared to the continuous-mode actuation. The velocity vectors indicate that a saddle point is located on the central axis in the near-wall region which separates the wall-normal jet and recirculation zone. The width of the recirculation zone near the central axis is higher in burst-mode actuation compared to the continuous-mode actuation.

Figure 9 shows the mean flow field behavior for selected cases of continuous-mode and burst-mode operation (two from each mode of operation) obtained from full-field measurements. Results are presented at $\phi_{pp} = 8.0$ kV and 9.8 kV for continuous-mode operation. In the burst mode, the results are presented for $f_b = 10$ Hz and 200 Hz with $\phi_{pp} = 8.0$ kV. The velocity vectors are superimposed on isocontours of vorticity ω normalized by its global maximum value ω_{\max} of respective cases. An isocontour line of $v/v_{\max} = 0.5$ is also superimposed on each plot to show the characteristics of jet half-width, $\delta_{1/2}$. The jet width decreases with an increase in actuation voltage from $\phi_{pp} = 8.0$ kV to 9.8 kV. The spreading of the jet is higher at lower actuation amplitude, $\phi_{pp} = 8.0$ kV. The symmetric distribution of vorticity about the central jet axis confirms the symmetry of the mean flow field, which is independent of actuation mode. However, asymmetric distribution of vorticity develops inside the recirculation zone for the actuation amplitude, $\phi_{pp} = 9.8$ kV, probably due to random behavior of recirculation vortex as discussed earlier. The jet spreading is significantly higher for the burst-mode operation at $f_b = 10$ Hz due to the formation of large periodic vortices. At higher burst frequency, $f_b = 200$ Hz, the flow field in burst mode approaches its continuous-mode counterpart at $\phi_{pp} = 8.0$ kV (see Fig. 8). There is difference in nature of vorticity distribution and recirculation zone between continuous-mode and high-frequency burst-mode actuation. The magnitude of $\omega_{\max} = 293.0$ s⁻¹ in continuous mode is higher than $\omega_{\max} = 212.3$ s⁻¹ for burst mode at $f_b = 200$ Hz. The isocontour line of $v/v_{\max} = 0.5$ is wider for burst mode in comparison to continuous mode indicating higher jet width in burst-mode actuation.

Figure 10 shows the evolution of the v -velocity profile along the wall-normal direction for both continuous mode and burst mode by selecting one case from each of the operating modes. The actuation voltage is equal to 8 kV for both continuous- and burst-mode actuation. The burst frequency is equal to 10 Hz and $\alpha = 70\%$. Figure 10 demonstrates that the velocity profile develops starting from the near-wall region up to a distance $y/d_e \approx 0.3$ in the wall-normal direction. At further downstream locations, insignificant change in nature of the velocity profile is observed for both continuous mode and burst mode of operation. The velocity profile also demonstrates the symmetry of the flow field about the central axis. Some minor asymmetry is observed in the near-wall region, possibly due to the oscillation of the recirculation bubble. In comparison to continuous mode, burst mode shows a greater spread in the velocity profile. In the near-wall region ($y/d_e = 0.009$ to 0.049) and close to the exposed electrode ($x/d_e = +0.5$ to -0.5) the magnitude of negative v velocity is higher for the burst-mode actuation than the continuous mode, indicating higher entrainment of the fluid from the ambient region for the burst-mode actuation.

To understand the observation of Humble *et al.* [7], i.e., the complete flow reversal due to reduction in diameter d_e of the annular actuator, Borradaile *et al.* [39] simulated the actuator behavior for different values of actuator diameter. The developing velocity profile in the near-wall region in the present study correlates well with the simulation results of Borradaile *et al.* [39] for the cases of wall-normal jet. The decreasing magnitude of velocity near the origin in the velocity profile (see Figs. 4(a)–4(c) of Ref. [39]) can be attributed to the recirculation zone observed in the present investigation.

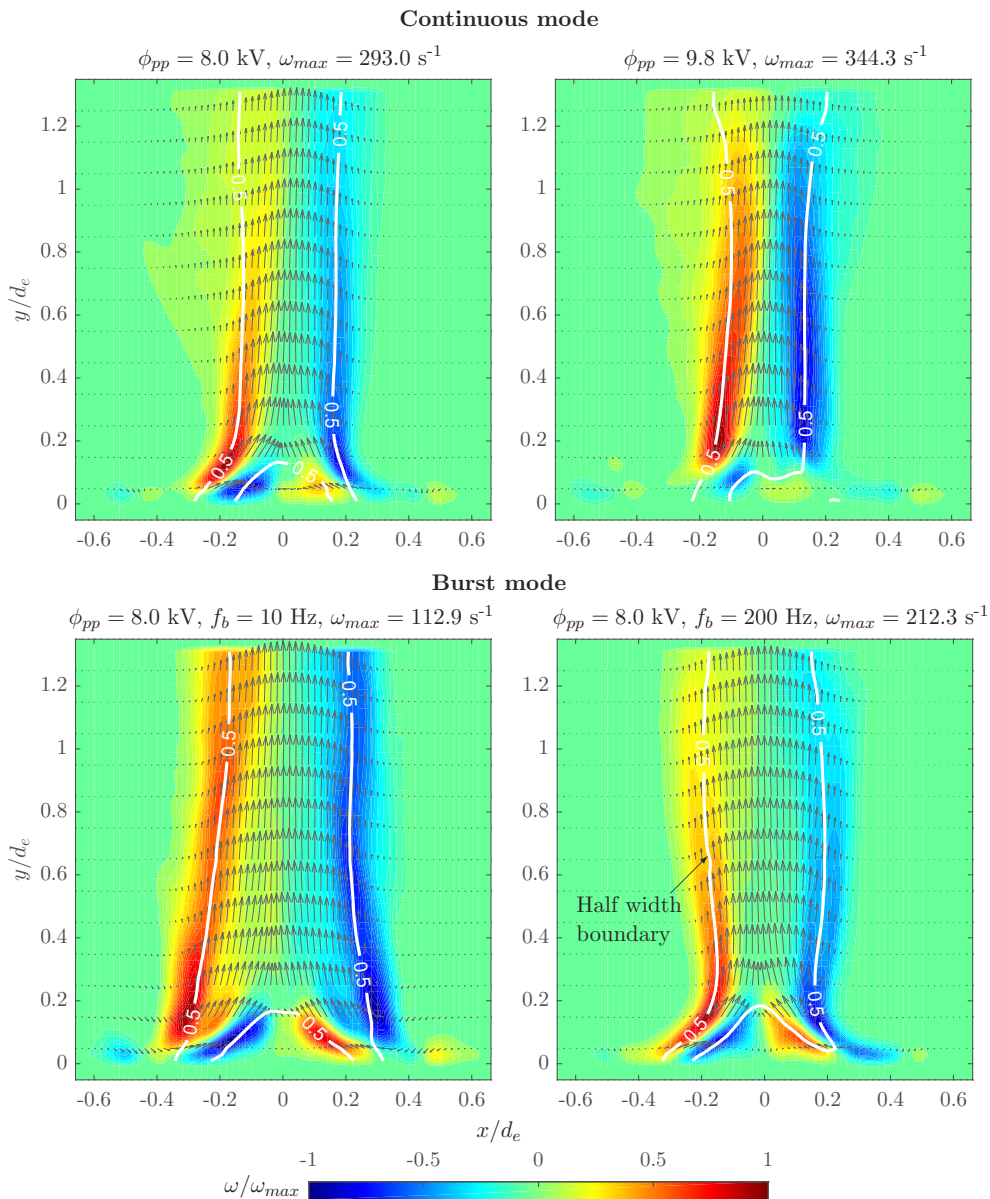


FIG. 9. Mean flow field in continuous mode and burst mode. The velocity vectors are superimposed on isocontours (shown by color map) of nondimensional vorticity, $\omega/|\omega_{max}|$. An isocontour of v/v_{max} (shown by white line with label) shows the spatial variation of half-width along the wall-normal direction.

1. Self-similar behavior

The present section evaluates the self-similar behavior of the cross-stream mean axial velocity profile of the induced wall-normal jet. A qualitative idea about the self-similar behavior can be made by comparing the axial velocity profile (see Fig. 10) for both continuous and burst mode of actuation. The self-similarity in axial velocity of the wall-normal jet is demonstrated by normalizing the time-averaged axial velocity v by its local maximum v_{max} and normalizing the radial position x

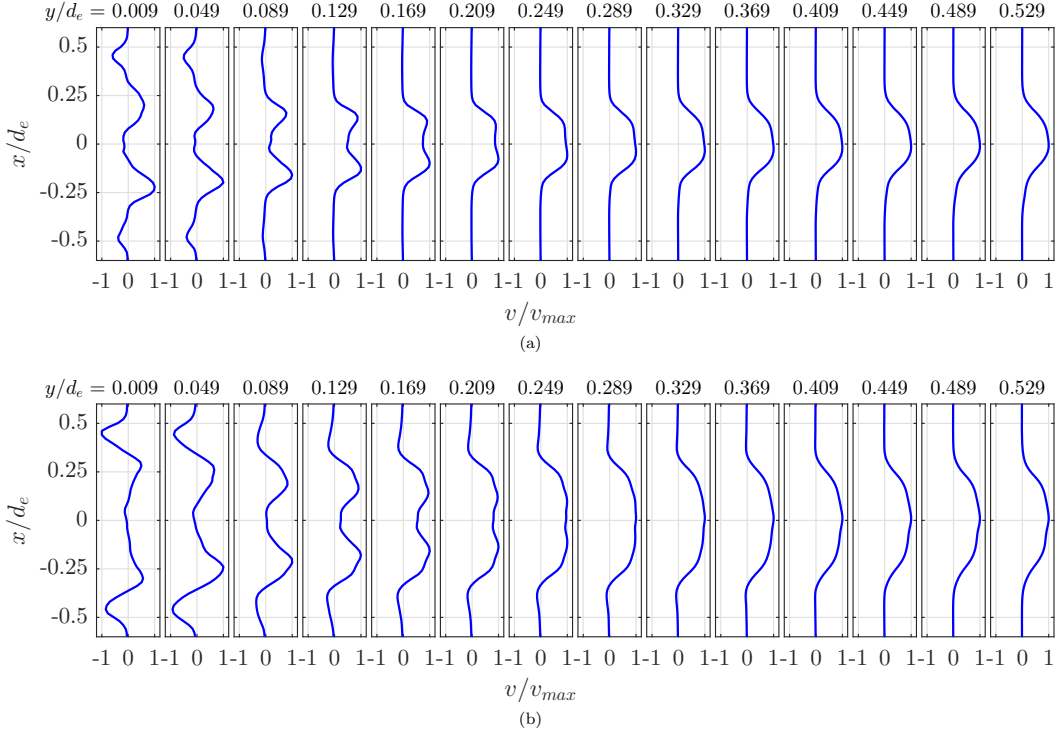


FIG. 10. Spatial evolution of v -velocity profile normalized with localized maxima in v velocity, v_{\max} , from near-wall region (y/d_e) = 0.009 to a self-similar region (y/d_e) > 0.369 (a) continuous mode $\phi_{pp} = 8$ kV and (b) burst mode $\alpha = 70\%$, $f_b = 10$ Hz, and $\phi_{pp} = 8$ kV.

with d_e . The dual-peak behavior transforms to a single-peak profile for $y/d_e > 0.329$. The spread or bandwidth of the velocity profile is higher for burst-mode actuation compared to the continuous-mode actuation. Figure 11(a) shows the velocity profile at 16 streamwise locations, i.e., from $y/d_e = 0.368$ to 1.268 with a constant step size of $y/d_e = 0.06$, for all actuation conditions, i.e., cases 1 to 13 (see Table I). Figure 11(b) shows the velocity profile for all these cases superposed together at two locations, i.e., $y/d_e = 0.43$ (near downstream) and $y/d_e = 1.23$ (far downstream). The normalized velocity profile collapses to a single curve for all the cases with minor scatter. It confirms the self-similarity of velocity profile for all the actuation conditions at axial locations, $y/d_e > 0.4$.

It may be noted that the self-similar velocity profile of the turbulent free jet and conventional synthetic jet follows a well-defined exponential function [40–43]. The velocity profile for the present case is approximated with an exponential function considering the basis of turbulent jet velocity profile as

$$\frac{v}{v_{\max}} = e^{-c(x/d_e)^2}, \quad (2)$$

where c is a constant. The curve-fitted velocity profile has been presented in Figs. 11(a) and 11(b) using the value of $c = 28$. The solid line shows the curve fit, which shows a close match with the experimental data. Figure 11(b) shows the success of the curve fit for all actuation conditions by comparing experimental data at close to upstream region, $y/d_e = 0.43$, and far downstream region, $y/d_e = 1.23$. It may be noticed that a single value of constant c has been used. Minor modification in the value of c can match with the individual cases better. The good match of the curve-fitted plot with all experimental velocity profiles indicates insignificant effect of actuation conditions on the self-similar behavior of the wall-normal jet generated by annular DBD plasma actuator. Namer and

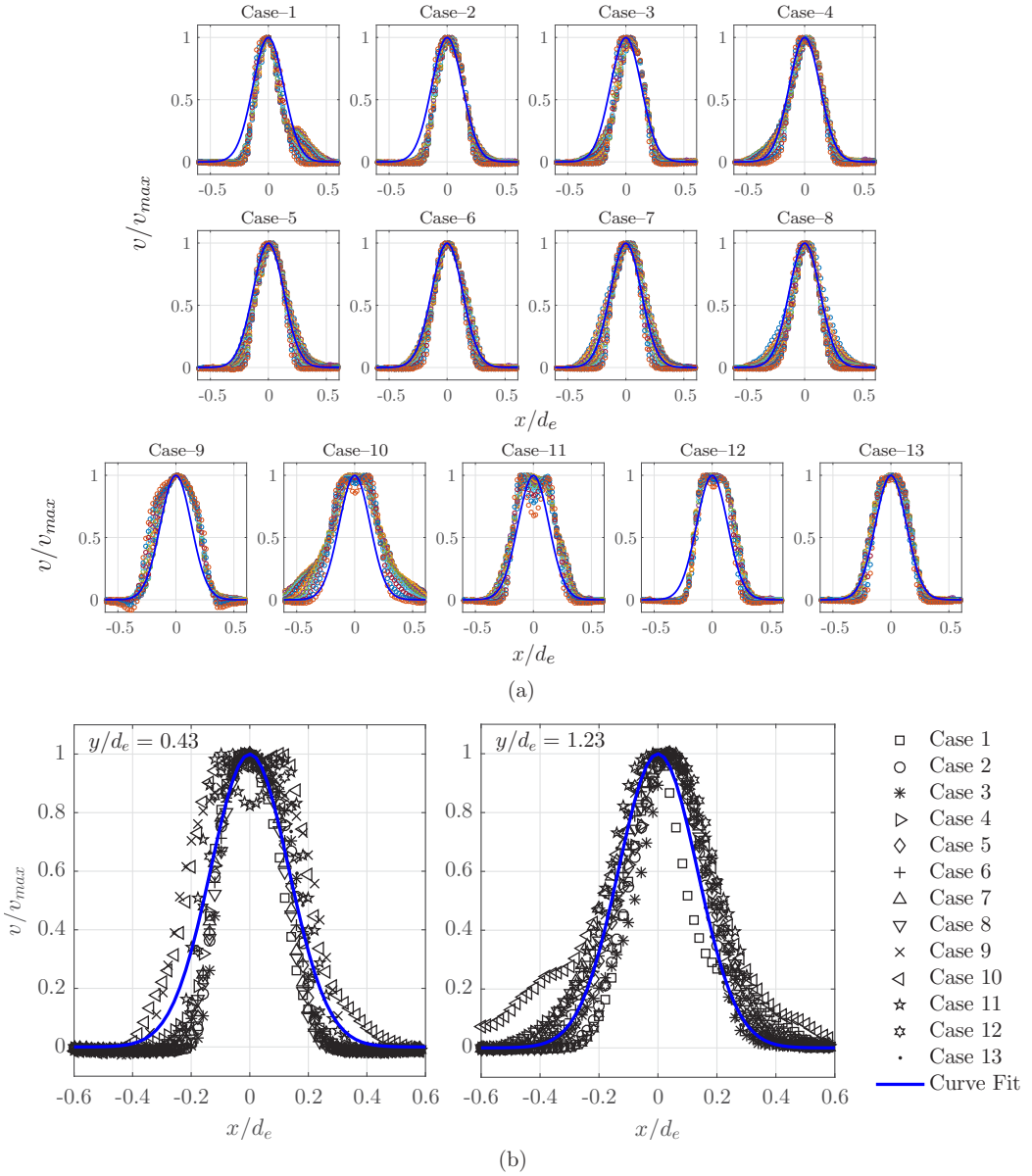


FIG. 11. (a) Nondimensional wall-normal velocity profile, v/v_{max} , in self-similar region along the radius (x direction) of annulus, extracted from the mean flow field at 16 stations in y direction from $y/d_e = 0.368$ to 1.268 with a constant step size of $y/d_e = 0.06$, in continuous mode from case 1 to 8 and in burst mode from case 9 to 13. The solid line corresponds to an approximated exponential distribution, $v/v_{max} = e^{-c(x/d_e)^2}$, with the value of $c = 28$, and (b) ensemble of velocity profile from all test cases at two different streamwise locations, $y/d_e = 0.43$ and 1.23 (far downstream), along with same curve fit as in (a).

Ötügen [40] also observed the value of constant c to be independent of Re . They used $c = \ln(2)$ and the radial distance was normalized by the jet half-width. Thomas *et al.* [41] used the value of $c = 94$ when the radial distance was normalized by the axial distance.

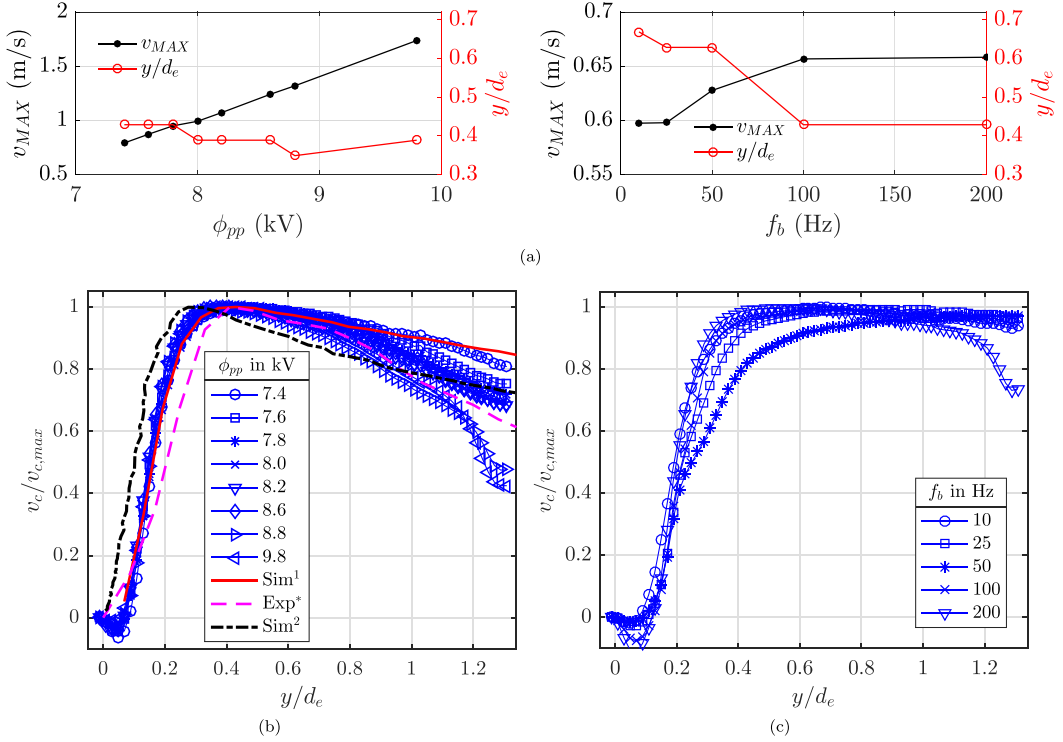


FIG. 12. (a) The absolute maximum of axial velocity, v_{max} , considered as characteristic velocity of induced flow as a function of increasing values of ϕ_{pp} in continuous mode (left), and for increasing values of f_b in burst mode (right). The evolution of axial velocity along the central axis, v_c , showing the acceleration and decay of induced flow in (b) continuous mode as a function of increasing values of ϕ_{pp} , and (c) burst mode ($\phi_{pp} = 8.0$ kV) as a function of increasing values of f_b . In continuous mode, the evolution of v_c is compared with the experiment (Exp*) [5], and simulations (Sim¹) [5] and (Sim²) [23]. The simulation results correspond to simulation of a 2D wall-normal jet generated by L-DBD-PSJA. The distance between exposed electrode edge of the L-DBD-PSJA is taken as d_e which is equal to 12.7 mm. The magnitude of v_c is normalized by its maximum value, $v_{c,max}$.

D. Mean flow statistics

Figure 12(a) shows the variation in global maximum of wall-normal velocity, v_{max} , and its corresponding streamwise location as a function of actuation voltage, ϕ_{pp} , for continuous-mode actuation and burst frequency, f_b , in burst-mode actuation, respectively. An increase in ϕ_{pp} leads to increase in the magnitude of v_{max} which is a direct consequence of actuation voltage versus body force relationship. In comparison to ϕ_{pp} , increase in burst frequency produces a very small increase in v_{max} in a limited frequency range between $f_b = 25$ Hz to 100 Hz. There is no change in v_{max} for $f_b > 100$ Hz indicating similar dynamics of induced flow at high burst frequency. It may be noted that $v_{max} = 1$ m/s for continuous mode compared to 0.68 m/s at $f_b = 200$ Hz for burst-mode actuation. This may be attributed to greater spread of the wall-normal jet in the streamwise direction for burst-mode actuation compared to the continuous-mode actuation. The effect of ϕ_{pp} on the location of v_{max} is very small for the continuous-mode actuation [see Fig. 12(a)]. The location of v_{max} shifts toward the wall with increase in f_b till $f_b = 100$ Hz in the burst-mode actuation. The location of v_{max} is observed at the same streamwise location ($y/d_e = 0.4$) for higher burst frequency as that of continuous-mode actuation.

Figures 12(b) and 12(c) show the evolution of centerline velocity, v_c , for continuous mode and burst mode as a function of ϕ_{pp} and f_b , respectively. The values of v_c are negative very close to wall (below $y/d_e \approx 0.15$). The negative values of v_c indicate the presence of a recirculation zone near the actuator surface. The flow is accelerated to a peak value within a short distance of $y/d_e \approx 0.4$ from the actuator surface and the value of v_c increases until it becomes equal to v_{\max} . Subsequently, there is a drop in velocity maxima, v_{\max} , in the downstream direction for all settings of actuation voltage ϕ_{pp} . The rate of deceleration in local maxima of velocity increases with increase in actuation voltage. The effect of f_b on evolution of v_{\max} velocity along the centerline is shown in Fig. 12(c) which has a similar trend, i.e., acceleration of fluid followed by decay of v_c after reaching the maxima. However, the decay is slower for the burst mode compared to the continuous mode of operation. This may be attributed to the difference in the nature of vortical structures inside the self-similar region of the wall-normal jet, which will be presented in a later section. It may be noted that v_{\max} does not occur on the jet centerline in the near-wall region due to the presence of the recirculation zone followed by a flow development zone. The local maximum of velocity v_{\max} always occurs on the jet centerline downstream from the location of v_{\max} . Thus, the decay of v_{\max} starting from the location of y at v_{\max} can also be treated as decay of v_c . Consequently, v_{\max} can be replaced by v_c in Eq. (2) and rewritten as

$$\frac{v}{v_c} = e^{-c(x/d_e)^2}. \quad (3)$$

The evolution of v_c from the present experiment is compared with the experimental and simulation results of Santhanakrishnan *et al.* [5] and simulation results of Ibrahim and Skote [23]. The experimental results of Santhanakrishnan *et al.* [5] do not match well with their simulation results in the downstream region. Our experimental results show a negative centerline velocity in the near-wall region [see Fig. 12(b)] contrary to the simulation and experimental results available in the literature [5,23]. The negative value of v_c corresponds to the recirculation bubble. The simulation of Ibrahim and Skote [23] shows a better match to experimental results of Santhanakrishnan *et al.* [5] in the far downstream region and a poor match in the near-wall region. In contrast, we see that in the near-wall region, the numerical simulation results of Santhanakrishnan *et al.* [5] have a better match to our experimental results at all values of ϕ_{pp} except in the immediate vicinity of the actuator surface compared to their experiment. In the near-wall region, the normalized velocity profile is independent of the actuation amplitude. For the low value of $\phi_{pp} = 7.4$ kV, the simulation results of Santhanakrishnan *et al.* [5] also show a good match with our experimental result in the far-field region. The simulation of Ibrahim and Skote [23] also compares well at moderate values of ϕ_{pp} in the far downstream region. However, for greater values of $\phi_{pp} = 8.8$ and 9.8 kV, both the models fail to predict our experimental data accurately in the far downstream regions. It may be recalled that higher values of ϕ_{pp} correspond to higher Re, and departure of simulation results at higher actuation amplitude can be attributed to the Reynolds number effect.

Figure 12(c) shows that negative values of v_c spread up to a larger extent, $0.1 < y/d_e < 0.15$, in burst-mode actuation compared to continuous mode. This may be attributed to different size of the recirculation zone and separation point for continuous mode compared to burst mode of operation. The magnitude of v_c in the recirculation region is greater for $f_b = 100$ Hz and 200 Hz because at low values of f_b the formation of the recirculation zone is comparatively more intermittent in nature. The decay of v_c is slower for the low values of burst frequency ($f_b < 100$ Hz) which may be attributed to weaker flow velocity of periodic vortex. At $f_b = 200$ Hz, for $y/d_e > 1.0$ there is a faster decay of v_c compared to rest of the cases. This fast decay of centerline velocity at $f_b = 200$ Hz is similar to the continuous mode actuation at $\phi_{pp} = 8.0$ kV. It indicates that the nature of flow field approaches to continuous mode at higher values of burst frequency, f_b .

E. Entrainment coefficient

The mass entrainment characteristic of A-DBD-PSJA is reported in this section for different mode of actuation and compared with the SparkJet actuator. Hussein *et al.* [44] reported the

entrainment coefficient, ζ , of a self-similar jet as

$$\zeta = \frac{1}{2} \frac{I_1}{\sqrt{I_2}}, \quad (4)$$

where the quantities I_1 and I_2 in Eq. (4) are defined as

$$I_1 = 2 \int_0^\infty \frac{v}{v_c} \eta d\eta, \quad I_2 = 2 \int_0^\infty \left(\frac{v}{v_c}\right)^2 \eta d\eta. \quad (5)$$

Here, $\eta = x/y$ is the similarity variable, where x is the radial distance, and y is the streamwise distance. The values of ζ are reported from the average of calculations performed at three different downstream locations. The entrainment coefficient ranges from 0.13 to 0.18 for the continuous-mode actuation and 0.16 to 0.29 for the burst-mode actuation. A similar order of entrainment constant, $\zeta = 0.19$ to 0.26, has been reported by Zong and Kotsonis [14] for the SparkJet actuator operating at a discharge frequency of 50 Hz to 200 Hz. A close match of ζ with the values reported by Zong and Kotsonis [14] can be attributed to the pulse-mode operation of the SparkJet actuator. The highest value of $\zeta = 0.29$ is found for the burst frequency of 25 Hz. In the continuous mode the highest value of $\zeta = 0.18$ is found at $\phi_{pp} = 8.0$ kV. We observed an increasing trend from ζ for increasing value of ϕ_{pp} up to $\phi_{pp} = 8.0$ kV. For further increase in the ϕ_{pp} , the value of ζ comes down and becomes nearly constant. The behavior of ζ with respect to burst frequency, f_b , is similar to that of ϕ_{pp} .

F. Coherent structures

Apart from the starting vortex and static recirculation vortex inside the recirculation region, regular vortical structures are observed inside the wall-normal jet due to roll-up of the shear layer at the boundary of the wall-normal jet. This can be visualized and confirmed from a sequence of visualization images. The second invariant of velocity gradient tensor known as the Q criterion can be used to identify the vortical structure. The positive value of Q identifies the vortex and the negative part describes the strain. The Q criterion can be evaluated from the two-dimensional data using $Q = 0.5(\partial u/\partial y)(\partial v/\partial x)$ [45–47]. Figure 13 shows the isocontours of positive values of the Q criterion as a function of actuation voltage amplitude, ϕ_{pp} , for continuous mode of actuation. For the lowest value of $\phi_{pp} = 7.4$ kV, a lower number of vortices are formed with comparatively lower strength. The number of vortices and their strength increases with increasing applied potential. At higher actuation voltage ($\phi_{pp} = 8.8$ kV and 9.8 kV), a greater number of vortices are formed indicating higher turbulence of the wall-normal jet. The strength of vortices weakens in the downstream region at low actuation voltages ($\phi_{pp} = 7.4$ kV and 8.0 kV). However, at higher actuation voltages ($\phi_{pp} = 8.8$ kV and 9.8 kV) the strength of vortices remains strong in the entire flow field region. The multimedia view provided for Fig. 13 clearly shows the shear layer roll-up and vortex generation. These random vortices are responsible for forming a turbulent wall-normal jet. A high Q value in the near-wall region ($x/d_e \simeq 0.22$, $y/d_e \simeq 0.18$) is attributed to turning of the approach flow toward the center of the actuator in the wall-normal direction.

Figure 14 shows the instantaneous Q value at a random phase for the burst-mode operation. At $f_b = 10$ Hz, a large periodic vortex is formed which travels up to a larger distance in the wall-normal direction with sufficient strength. Two subsequent periodic vortices (marked as Π_{N-1} and Π_{N-2}) at $f_b = 10$ Hz remain separated by a sufficient distance without any mutual interaction. The spacing between subsequent vortices reduces (see at $f_b = 50$ Hz) and vortex size reduces with increase in burst frequency. At $f_b = 50$ Hz, the periodic vortices are diffused before reaching $y/d_e = 0.6$ and at a higher value of $f_b = 100$ Hz and 200 Hz, the vortices are diffused and merged even before $y/d_e = 0.2$ in the shear region. The movie in the Supplemental Material [48]. shows the formation of a large number of small vortical structures in the downstream region. The overall strength of these vortices is higher in continuous-mode excitation as compared to that of burst-mode excitation. The temporal features of these vortical structures are discussed in the next section (Sec. III G).

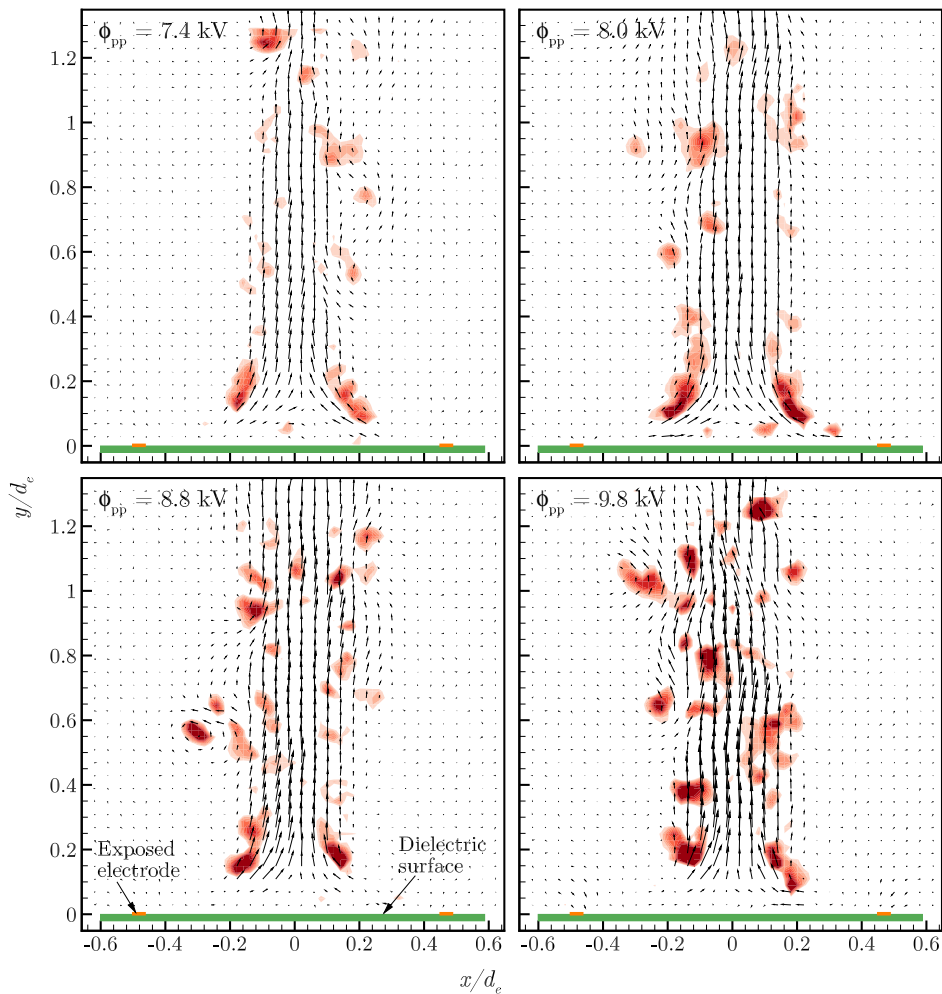


FIG. 13. Instantaneous Q value at a random phase in continuous mode showing the signature of vortices as a function of ϕ_{pp} : (a) 7.4 kV, (b) 8.0 kV, (c) 8.8 kV, and (d) 9.8 kV. The vortices are identified using Q criterion where only positive values of Q are plotted and the contour levels are kept the same in all the plots. The dielectric surface of actuator is shown by a large rectangle (green in color) and exposed electrode is shown by a tiny rectangle (orange in color). The multimedia view in the Supplemental Material [48] shows the dynamics of vortices using Q -value evolution.

G. Spectral characteristics

The fast Fourier transform (FFT) of the u - and v -velocity fluctuations is carried out for obtaining the spectral content of vortical structures. The data points acquired at a sampling rate of 1.25 kHz in the steady-flow and periodic-flow regimes, i.e., outside the starting vortex period, are used for the FFT calculation. The TR-PIV results from the measurement plane 1 (full-field) and measurement plane 2 (near-field) are used for spectral calculation. Figures 15 and 16(a) show the spatial evolution of spectra along the centerline in the streamwise direction from ($y/d_e = 0.05$ to 1.27) for continuous- and burst-mode actuation, respectively.

Figure 15(a) shows the u -velocity spectra for the continuous-mode actuation as a function of Reynolds number, Re_d (i.e., ϕ_{pp}). In the near-field region ($y/d_e < 0.6$), the average frequency of u -velocity fluctuation increases with increase in Reynolds number from 2620 to 4111 with subsequent

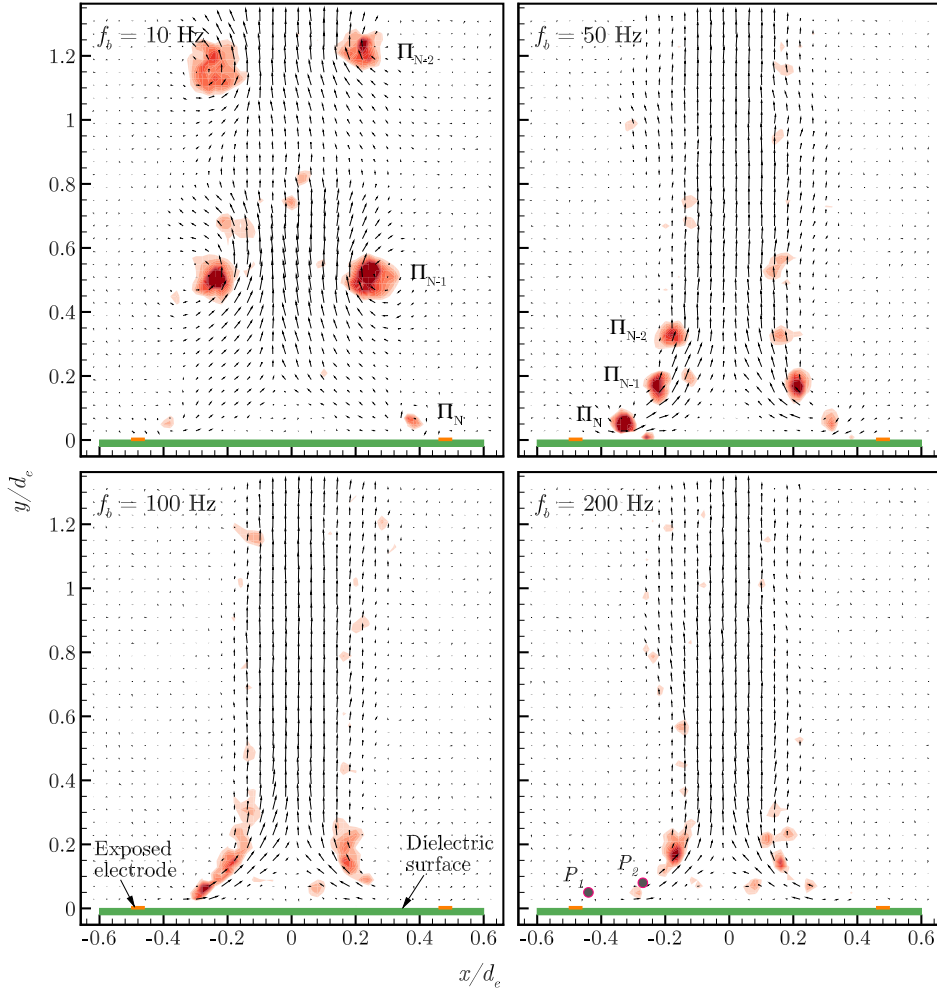


FIG. 14. Instantaneous Q value at a random phase in burst mode showing the signature of vortices as a function of f_b : (a) 10 Hz, (b) 50 Hz, (c) 100 Hz, and (d) 200 Hz. The vortices are identified using Q criterion where only positive values of Q are plotted and the contour levels are kept the same in all the plots. The dielectric surface of actuator is shown by a large rectangle (green in color) and exposed electrode is shown by a tiny rectangle (orange in color). The multimedia view in the Supplemental Material [48] shows the dynamics of vortices using Q -value evolution. The sequence of observable periodic vortex is marked as Π_N , Π_{N-1} , and Π_{N-2} . The points P_1 and P_2 show the locations used for the phase portrait presented in Fig. 17.

drop in magnitude at $Re_d = 5753$. It may be noted that we have observed different behavior of centerline velocity, v_c , in the downstream direction at higher actuation voltage, i.e., $\phi_{pp} = 8.8$ kV and 9.8 kV in Fig. 12(a). The difference in spectral behavior can be correlated with difference in nature of vortex structures at higher Reynolds number. The average amplitude of frequency content also increases with increase in Reynolds number from 2620 to 4111. The high-frequency content transforms to low-frequency content in the downstream region for Reynolds number range of 2620 to 4111. The average spectral content at $Re_d = 5753$ increases in the downstream direction indicating nonlinear interaction between the vortex structures.

The spectral content of v -velocity fluctuations shown in Fig. 15(b) indicates the dominance of low-frequency content in the far-field region ($y/d_e > 0.6$) and no dominant fluctuation in the

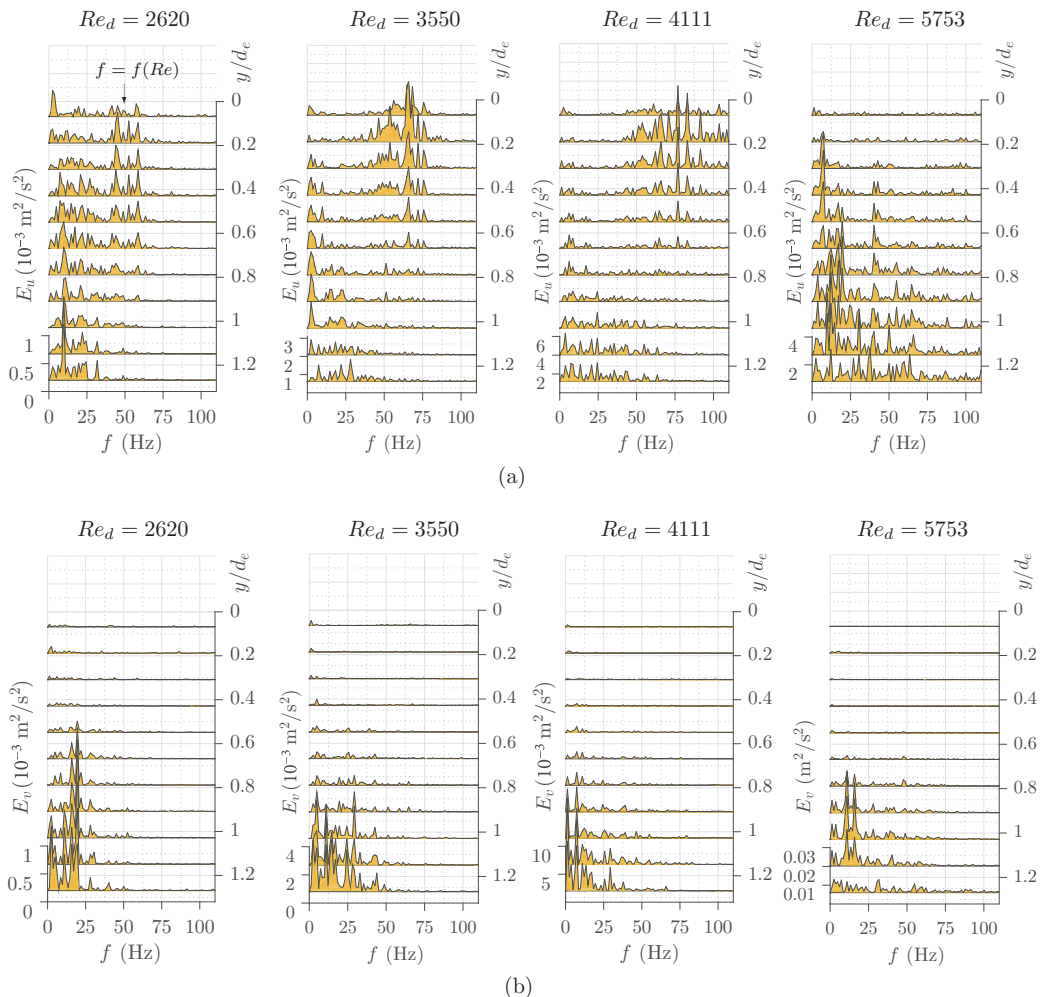


FIG. 15. Spectra from fluctuations of (a) u velocity and (b) v velocity along the centerline of wall-normal jet (y/d_e) as a function of Re_d for continuous mode actuation. The data points are collected from full-field measurement and the maximum range of f in each plot is restricted to 110 Hz since no observable spectral peak is present beyond this range.

near-field region ($y/d_e < 0.6$) for all actuation amplitude cases. The amplitude of v -velocity fluctuation spectra increases with increase in Reynolds number from $Re_d = 2620$ to 5753 . Hence, we can conclude that transverse oscillation of the recirculation bubble contributes to the fluctuation in the near-field region as evident from spectral content of v -velocity fluctuation. The presence of spectral content in both u - and v -velocity fluctuations in the downstream region indicates the formation of random vortex structures and interaction in the wall-normal jet for continuous-mode actuation. The spectral content behavior correlates well with the Q -value results shown in Fig. 13.

Figure 16(a) presents the spectra of v -velocity fluctuation as a function of burst frequency, f_b , at different streamwise locations, y/d_e , for burst-mode actuation. In comparison to continuous mode, the flow field in burst mode is generated due to an impulsive action of body force at the start of each burst cycle, which is periodic in the time interval of burst period, t_b . Figure 16(a) shows a clear frequency peak at $f = 10$ Hz for $f_b = 10$ Hz suggesting that at low values of f_b , vortex structures are

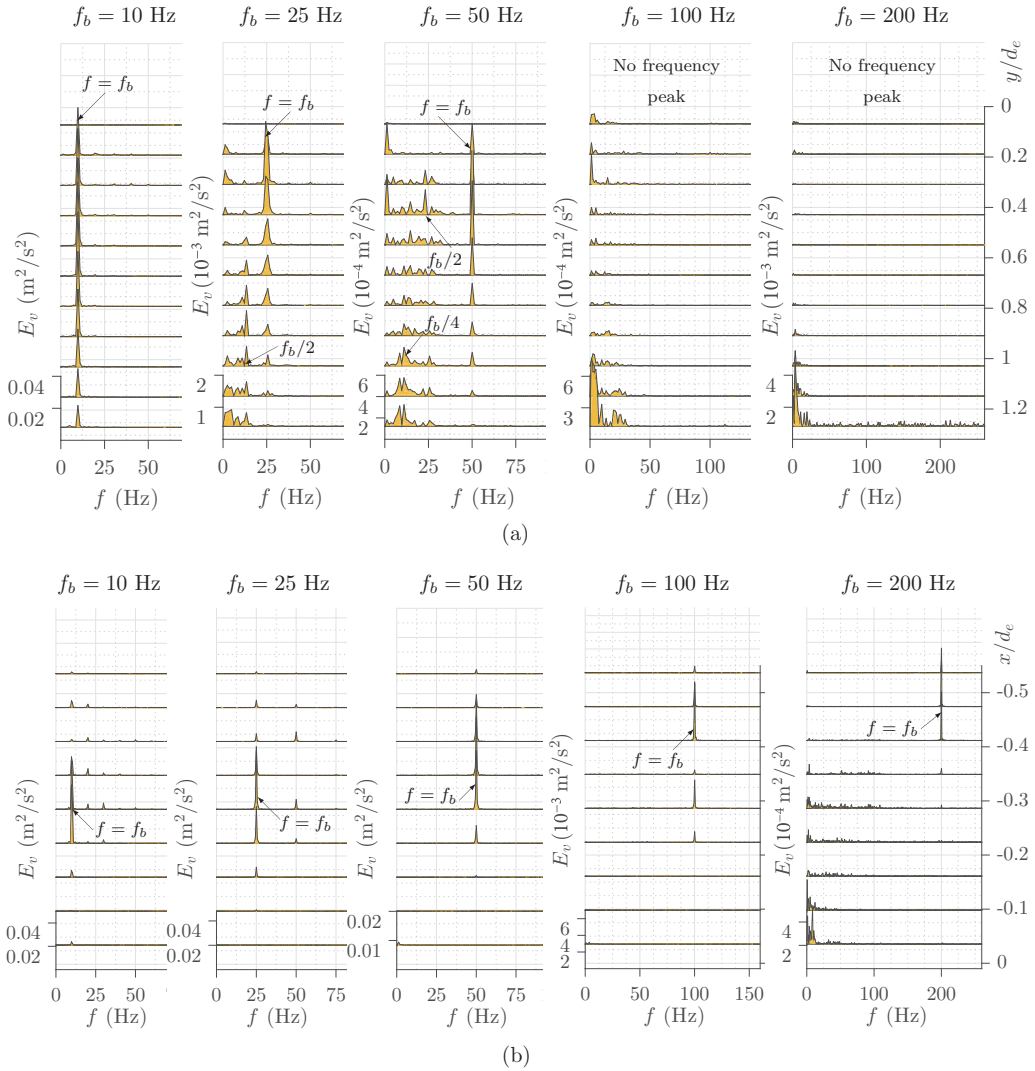


FIG. 16. Spectra from fluctuations of v velocity for burst mode actuation as a function of f_b (a) along the centerline of the wall-normal jet (y/d_e), and (b) along a line parallel to the wall (x/d_e) at $y = 2.4$. The data points for (a) and (b) are collected from full-field and near-field measurements, respectively. Notice the peaks of spectra are also locked in for $f_b = 100$ Hz and 200 Hz in the neighborhood region of the exposed electrode.

produced at burst frequency. There is no vortex merging and nonlinear interaction between vortical structures. The spacing between the vortices is large, as seen in the results of Q values in Fig. 14. At moderate value of burst frequency, $f_b = 25$ Hz, there is presence of a subharmonic frequency at $f = f_b/2 = 12.5$ Hz in between $y/d_e \approx 0.4$ to 1.2 along with a dominant peak at $f = 25$ Hz. At higher value of $f_b = 50$ Hz, two subharmonic modes appear one at $f = f_b/2$ and another at $f = f_b/4$. Hence, we can conclude that at moderate values of f_b merging of vortices takes place leading to the appearance of subharmonic modes. In burst mode, the bursting frequency dominates the wall-normal jet behavior, and spectral peaks remain locked with values of f_b . For $f_b = 100$ Hz and 200 Hz, no definite spectral peak is observed at the burst frequency. This indicates that shedding

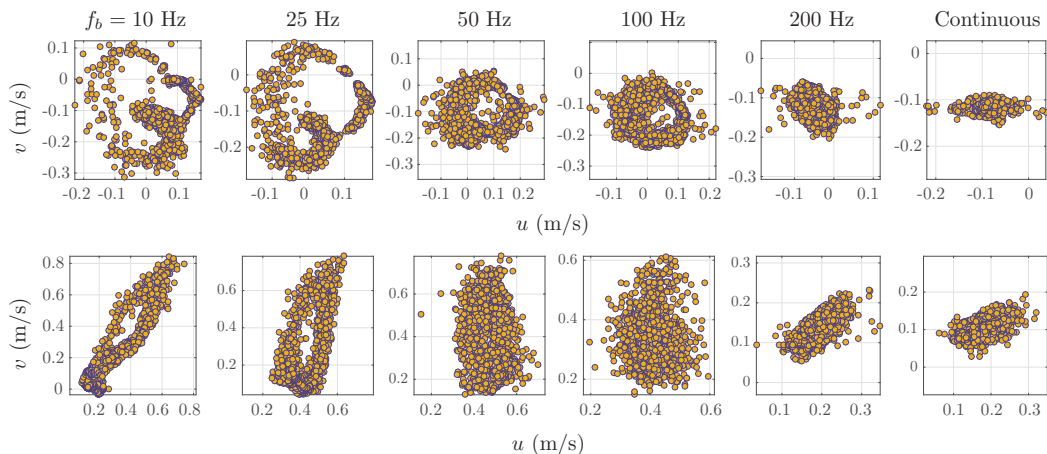


FIG. 17. The phase relationship between the u velocity and v velocity in near-wall region as a function of burst frequency f_b and in continuous-mode operation at two different locations: top row, near the exposed electrode ($x/d_e = -0.44$, $y/d_e = 0.05$), and bottom row, near the shear region ($x/d_e = -0.27$, $y/d_e = 0.08$). The locations are marked as point P_1 and P_2 in Q -value plot at $f_b = 200$ Hz (see Fig. 14).

in the shear layer of the wall-normal jet is incomplete at higher burst frequencies. This observation correlates well with the Q -value results presented in Fig. 14.

The spectral calculation along the centerline shows the absence of any clear dominant peak at burst frequency $f_b > 100$ Hz. In order to further investigate the flow structures at higher values of f_b , the FFT is calculated along the radial distance (x/d_e) just above the wall (at $y = 2.4$ mm) using the data from near-field measurements. The results are presented in Fig. 16(b). It reveals the presence of dominant frequency at all values of burst frequency, f_b , including $f_b = 100$ Hz and 200 Hz before the shear region, i.e., $x/d_e < -0.2$. The dominant frequency is locked with burst frequency, and the strength of frequency peak reduces with increase in burst frequency. At $f_b = 200$ Hz, dominant spectra are observed in close vicinity of the exposed electrode, i.e., $x/d_e = -0.5$ to -0.4 . It may also be noticed that the location of the spectral amplitude peak also shifts toward the exposed electrode with increasing burst frequency. The presence of frequency peak in this zone indicates that suction of fluid at the exposed electrode is periodic even at high burst frequency, i.e., at $f_b = 200$ Hz.

The observation that the flow field in the burst-mode actuation at high values of f_b approaches that of continuous-mode actuation is also evident from the phase portrait of velocity components. Figure 17 shows the phase relationship of the velocity components in the near-wall region as a function of f_b and compares with that of continuous-mode actuation. The data probe is placed at two different locations ($x/d_e, y/d_e$), near the exposed electrode ($-0.44, 0.05$) and near the shear region ($-0.27, 0.08$), marked in Fig. 14 as point P_1 and P_2 . Figure 17 shows that the phase portrait results of burst-mode actuation approach that of continuous mode with increase in burst frequency. Near the exposed electrode ($-0.44, 0.05$), for all the values of burst frequency, the phase portrait shows a periodic behavior that correlates well with the spectral results shown in Fig. 16(b). At $f_b = 200$ Hz, the phase portrait does not clearly show the cyclic character due to greater number of cycles. In this region ($-0.44, 0.05$), no phase portrait of burst-mode actuation matches with the continuous-mode phase portrait. The phase portraits of burst-mode actuation do not match with the continuous mode till $f_b \leq 100$ Hz in the region away from the exposed electrode, i.e., near the shear region ($-0.27, 0.08$) where the flow reversal takes place. At a higher value of burst frequency, $f_b = 200$ Hz, the phase portrait of burst-mode actuation closely resembles that of continuous-mode actuation. Therefore, it may be concluded that the burst frequency does not influence the nature of vortical structures in the wall-normal jet at high burst frequency. This behavior correlates well with

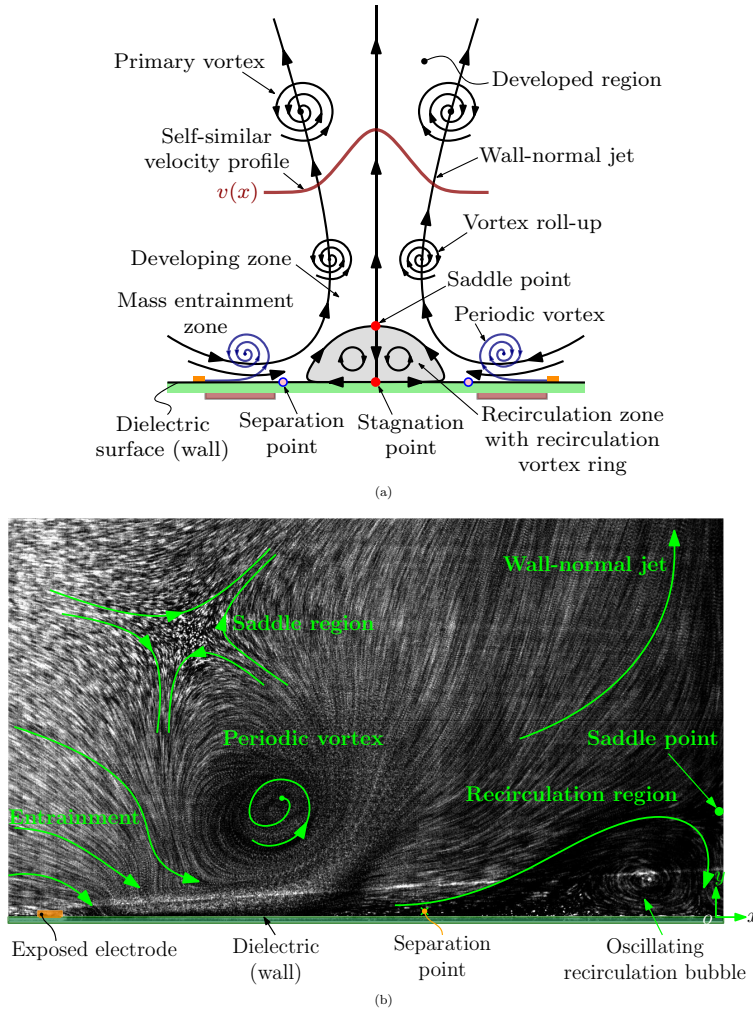


FIG. 18. The schematic describing the various features of flow field induced by an annular DBD plasma actuator (top), and flow topology in the near-wall region described using a sample instantaneous flow visualization image in burst mode (bottom).

the spectral results shown in Fig. 16(a), which shows no spectral peak for the burst-mode actuation at higher burst frequencies. Similarly, the Q -value plot shown in Fig. 14 also shows no definite vortex structure at high burst frequency. However, the effect produced by the higher values of f_b in the near-wall region cannot be discarded as it reflects in the mean behavior of the wall-normal jet as shown in Fig. 9.

H. Conceptual flow patterns

The wall-normal jet is a final outcome of the flow generated by A-DBD-PSJA, which is established after the occurrence of several complex events in the near-wall region. Figure 18 attempts to describe the flow features generated by the A-DBD-PSJA. Figure 18(a) shows the description of a typical mean flow field generated by an A-DBD-PSJA. The entire flow field developed during the actuation can be divided into four major regions: (i) mass entrainment zone, (ii) recirculation zone, (iii) developing zone, and (iv) self-similar region. The near-wall region contains the exposed

electrode, which is the source of plasma discharge toward the encapsulated electrode and hence the source of momentum. The flow is initiated from the neighborhood of the exposed electrode by entrainment. The momentum transfer with the surrounding fluid due to the ion transport takes place in the entrainment zone in the near-wall region. The discharge of plasma, entrainment of the fluid from the surroundings, formation of the starting vortex/periodic vortex, deflection of flow near the wall from the parallel direction to wall-normal direction, and recirculation bubble formation are the near-wall phenomena. The streamlines moving radially inward separate from the wall before meeting at the geometric center of the annular actuator and turn in the wall-normal direction to create a wall-normal jet. The wall boundary layer separation leads to the formation of a recirculation zone. The separated wall boundary layer rolls up, and a vortex ring is created inside the recirculation zone. The wall-normal jet and recirculation zone are separated by a saddle point. The wall-normal jet develops after the recirculation bubble region. In the developing zone, the flow develops to attain the peak velocity, and later it enters into a self-similar zone. In the self-similar zone, the flow field has a self-similar velocity profile similar to a plane free jet. The primary vortices formed due to shear layer roll-up (including the periodic vortices of burst-mode actuation) promote the turbulence of the free-jet-like flow.

Figure 18(b) shows an instantaneous flow visualization image at the near-wall region for the burst-mode actuation with annotated flow features. It demonstrates the mass entrainment zone near the exposed electrode, a periodic vortex generated by impulsive action and convecting toward the central axis, a moving saddle region on top of the periodic vortex created due to the interaction of periodic vortices, a recirculation region around the central axis, a saddle point on top of the recirculation zone separating the recirculation zone and wall-normal jet, and the wall-normal jet above the recirculation zone.

IV. CONCLUSION

The present study investigates the detailed flow field and vortical structures generated by an annular DBD plasma actuator in both continuous and burst mode of actuation. High-speed visualization and time-resolved PIV measurements have been carried out. Parametric studies on the effect of actuation amplitude (7.4 kV to 9.8 kV) and burst frequency (10 Hz to 200 Hz) have been carried out using both near-wall and far-field measurements. The duty cycle for burst-mode actuation is set at 70%. The Reynolds number based on the annulus diameter of the actuator varies in the range of 2620 to 5753 and 1978 to 2180 in continuous mode and burst mode of actuation, respectively. The results on starting vortex formation, periodic mean flow behavior, wall-normal jet characteristics, mean flow statistics, coherent structures, and spectral characteristics have been presented.

The mean flow field generated by the annular DBD plasma actuator consists of an entrainment zone near the exposed electrode, a vortex ring near the center of the annular actuator, and a free-jet-like flow normal to the actuator surface. The recirculation vortex ring is formed by the separation of the induced flow approaching from the exposed electrode toward the center of the actuator. The behavior of the recirculation bubble changes with increase in actuation voltage, ϕ_{pp} (equivalent to increasing Re), for continuous-mode actuation and burst frequency, f_b , for burst-mode actuation.

The average momentum of the wall-normal jet is higher in the continuous-mode actuation than in the burst-mode actuation. The average recirculation bubble size is larger in burst-mode actuation compared to the continuous-mode actuation indicating greater mixing for the former. The entrainment coefficient of burst-mode actuation is higher than that of continuous-mode actuation. The jet half-width of the wall-normal jet is also higher in burst-mode actuation compared to the continuous mode. The mean velocity profile of the wall-normal jet is self-similar in the far-field region with exponential velocity profile similar to that of free jet irrespective of the operating mode of the actuator. The development of absolute maximum of axial velocity in the wall direction of the annular DBD actuator (A-DBD-PSJA) is similar to that of the linear DBD actuator (L-DBD-PSJA). The successful comparison of the average velocity results from the present experimental results

with the simulation results confirms the potential of the modified Suzen-Huang model for design and analysis of the DBD plasma actuator [5,23].

The vortical structures are formed due to the roll-up of the shear layer of the wall-normal jet. The nature of vortices is different between continuous and burst modes of operation. Random vortices are shed in the low-frequency range for the continuous-mode actuation, which is a function of actuation amplitude. The strength and bandwidth of vortical structures increase with increase in the actuation amplitude. The vortices generated in the burst mode of actuation are locked in with burst frequency at the low-frequency range. The flow behavior approaches that of the continuous-mode actuation at high burst frequency.

Overall, the present study demonstrates the complexity of flow field generated by an annular DBD actuator using high-resolution time-resolved measurements. The design and operational parameter of an annular DBD plasma actuator can be tuned according to the design requirement. The A-DBD-PSJA is an effective device for flow control application. The results from the present study can be useful for design of different flow control applications.

The data that support the findings of this study are available from the corresponding author upon reasonable request.

-
- [1] S. Roy and C.-C. Wang, Bulk flow modification with horseshoe and serpentine plasma actuators, *J. Phys. D* **42**, 032004 (2009).
 - [2] C.-C. Wang and S. Roy, Combustion stabilization using serpentine plasma actuators, *Appl. Phys. Lett.* **99**, 041502 (2011).
 - [3] M. Riherd and S. Roy, Serpentine geometry plasma actuators for flow control, *J. Appl. Phys.* **114**, 083303 (2013).
 - [4] G. Neretti, A. C. Ricchiuto, and C. A. Borghi, Measurement of the charge distribution deposited by an annular plasma synthetic jet actuator over a target surface, *J. Phys. D* **51**, 324004 (2018).
 - [5] A. Santhanakrishnan, D. A. Reasor, and R. P. LeBeau, Characterization of linear plasma synthetic jet actuators in an initially quiescent medium, *Phys. Fluids* **21**, 043602 (2009).
 - [6] A. Santhanakrishnan and J. Jacob, On plasma synthetic jet actuators, in *44th AIAA Aerospace Sciences Meeting and Exhibit* (AIAA, 2006).
 - [7] R. A. Humble, S. A. Craig, J. Vadyak, P. D. McClure, J. W. Hofferth, and W. S. Saric, Spatiotemporal structure of a millimetric annular dielectric barrier discharge plasma actuator, *Phys. Fluids* **25**, 017103 (2013).
 - [8] G. Neretti, P. Seri, M. Taglioli, A. Shaw, F. Iza, and C. A. Borghi, Geometry optimization of linear and annular plasma synthetic jet actuators, *J. Phys. D* **50**, 015210 (2017).
 - [9] K.-S. Choi and J.-H. Kim, Plasma virtual roughness elements for cross-flow instability control, *Exp. Fluids* **59**, 159 (2018).
 - [10] K. Grossman, C. Bohdan, and D. VanWie, Sparkjet actuators for flow control, in *41st Aerospace Sciences Meeting and Exhibit* (AIAA, 2003).
 - [11] B. Z. Cybyk, D. H. Simon, H. B. Land, III and J. T. Wilkerson, Sparkjet actuators for flow control, Tech. Rep. No. ADA466100, Johns Hopkins University, 2007.
 - [12] H. S. Ko, S. J. Haack, H. B. Land, B. Cybyk, J. Katz, and H. J. Kim, Analysis of flow distribution from high-speed flow actuator using particle image velocimetry and digital speckle tomography, *Flow Meas. Instrum.* **21**, 443 (2010).
 - [13] L. Wang, Z. Xun Xia, Z. Bing Luo, and J. Chen, Three-electrode plasma synthetic jet actuator for high-speed flow control, *AIAA J.* **52**, 879 (2014).
 - [14] H. Zong and M. Kotsonis, Formation, evolution and scaling of plasma synthetic jets, *J. Fluid Mech.* **837**, 147 (2018).
 - [15] S. Huang, Z. Zhang, H. Song, Y. Wu, Z. Sun, and Y. Li, Analytic model and the influence of actuator number on the performance of plasma synthetic jet actuator array, *Appl. Sci.* **8**, 1534 (2018).

- [16] A. Santhanakrishnan, J. Jacob, and Y. Suzen, Flow control using plasma actuators and linear/annular plasma synthetic jet actuators, in *3rd AIAA Flow Control Conference* (AIAA, 2006).
- [17] A. Santhanakrishnan and J. D. Jacob, Flow control with plasma synthetic jet actuators, *J. Phys. D* **40**, 637 (2007).
- [18] A. Santhanakrishnan, Characterization and flow physics of plasma synthetic jet actuators, Ph.D. thesis, University of Kentucky, 2007.
- [19] A. Santhanakrishnan, D. Reasor, and R. LeBeau, Unstructured numerical simulation of experimental linear plasma actuator synthetic jet flows, in *46th AIAA Aerospace Sciences Meeting and Exhibit* (AIAA, 2008).
- [20] Y. Suzen, G. Huang, J. Jacob, and D. Ashpis, Numerical simulations of plasma based flow control applications, in *35th AIAA Fluid Dynamics Conference and Exhibit* (AIAA, 2005).
- [21] A. B. Liu, P. F. Zhang, B. Yan, C. F. Dai, and J. J. Wang, Flow characteristics of synthetic jet induced by plasma actuator, *AIAA J.* **49**, 544 (2011).
- [22] W. Shyy, B. Jayaraman, and A. Andersson, Modeling of glow discharge-induced fluid dynamics, *J. Appl. Phys.* **92**, 6434 (2002).
- [23] I. H. Ibrahim and M. Skote, Simulations of the linear plasma synthetic jet actuator utilizing a modified Suzen-Huang model, *Phys. Fluids* **24**, 113602 (2012).
- [24] T. Segawa, H. Yoshida, S. Takekawa, T. Jukes, and K.-S. Choi, Coaxial annular jet produced by DBD plasma actuator, *J. Jpn. Soc. Fluid Mech.* **27**, 65 (2008).
- [25] B. K. Mishra and P. K. Panigrahi, Video: Starting vortex, wall jet, periodic vortex and dipole generated by a dielectric barrier discharge plasma actuator in quiescent air, in *70th Annual Meeting of the APS Division of Fluid Dynamics—Gallery of Fluid Motion* (APS, 2017).
- [26] C. A. Borghi, A. Cristofolini, G. Neretti, P. Seri, A. Rossetti, and A. Talamelli, Duty cycle and directional jet effects of a plasma actuator on the flow control around a NACA0015 airfoil, *Meccanica* **52**, 3661 (2017).
- [27] B. K. Mishra and P. K. Panigrahi, Video: Coaxial jet excited by DBD plasma actuator, in *72th Annual Meeting of the APS Division of Fluid Dynamics—Gallery of Fluid Motion* (APS, 2019).
- [28] B. K. Mishra and P. K. Panigrahi, Design and characterization of a novel dielectric barrier discharge plasma actuator for flow control application, in *Fluid Mechanics and Fluid Power—Contemporary Research* (Springer, India, 2016), pp. 1545–1554.
- [29] B. K. Mishra and P. K. Panigrahi, Formation and characterization of the vortices generated by a DBD plasma actuator in burst mode, *Phys. Fluids* **29**, 024104 (2017).
- [30] B. K. Mishra and P. K. Panigrahi, Flow field induced by a dielectric barrier discharge plasma actuator analyzed with bi-orthogonal decomposition, *Phys. Fluids* **32**, 087112 (2020).
- [31] M. Hamdi, M. Havet, O. Rouaud, and D. Tarlet, Comparison of different tracers for PIV measurements in EHD airflow, *Exp. Fluids* **55**, 1702 (2014).
- [32] C. Gouriou, P. Traore, and C. Louste, Influence of seeding particle type on velocity measurements in silicone oil under high voltage, *IEEE Trans. Ind. Appl.* **53**, 2471 (2017).
- [33] W. Kim, H. Do, M. G. Mungal, and M. A. Cappelli, On the role of oxygen in dielectric barrier discharge actuation of aerodynamic flows, *Appl. Phys. Lett.* **91**, 181501 (2007).
- [34] J. Kriegseis, Performance characterization and quantification of dielectric barrier discharge plasma actuators, Ph.D. thesis, Technischen Universität Darmstadt, 2011.
- [35] X. Zhang and H. Zong, Vortex shedding frequency scaling of coherent structures induced by a plasma actuator, *AIAA J.* **60**, 1067 (2021).
- [36] B. McKeon, G. Comte-Bellot, J. Foss, J. Westerweel, F. Scarano, C. Tropea, J. Meyers, J. Lee, A. Cavone, R. Schodl, M. Koochesfahani, Y. Andreopoulos, W. Dahm, J. Mullin, J. Wallace, P. Vukoslavčević, S. Morris, E. Pardyjak, and A. Cuerva, Velocity, vorticity, and Mach number, in *Springer Handbook of Experimental Fluid Mechanics*, edited by Cameron Tropea, Alexander L. Yarin, and John F. Foss (Springer, Berlin, 2007), pp. 215–471.
- [37] B. K. Mishra and P. K. Panigrahi, Effect of duty cycle on flow induced by a dielectric barrier discharge plasma actuator in burst mode, in *7th International and 45th National Conference on Fluid Mechanics and Fluid Power (FMFP)* (National Society for Fluid Mechanics and Fluid Power, 2018).

- [38] R. D. Whalley and K.-S. Choi, The starting vortex in quiescent air induced by dielectric-barrier-discharge plasma, *J. Fluid Mech.* **703**, 192 (2012).
- [39] H. Borradaile, K. Kourtzanidis, F. Rogier, K.-S. Choi, and X. Mao, Flow reversal in millimetric annular DBD plasma actuator, *J. Phys. D* **54**, 345202 (2021).
- [40] I. Namer and M. V. Ötügen, Velocity measurements in a plane turbulent air jet at moderate Reynolds numbers, *Exp. Fluids* **6**, 387 (1988).
- [41] J. D. Thomas, C. M. Liu, F. A. Flachskampf, J. P. O'Shea, R. Davidoff, and A. E. Weyman, Quantification of jet flow by momentum analysis: An *in vitro* color Doppler flow study, *Circulation* **81**, 247 (1990).
- [42] J. Lee, T. Lu, H. Sun, and G. Miao, A novel formula to describe the velocity profile of free jet flow, *Arch. Appl. Mech.* **81**, 397 (2011).
- [43] B. L. Smith and A. Glezer, The formation and evolution of synthetic jets, *Phys. Fluids* **10**, 2281 (1998).
- [44] H. J. Hussein, S. P. Capp, and W. K. George, Velocity measurements in a high-Reynolds-number, momentum-conserving, axisymmetric, turbulent jet, *J. Fluid Mech.* **258**, 31 (1994).
- [45] M. S. Chong, A. E. Perry, and B. J. Cantwell, A general classification of three-dimensional flow fields, *Phys. Fluids* **2**, 765 (1990).
- [46] J. Jeong and F. Hussain, On the identification of a vortex, *J. Fluid Mech.* **285**, 69 (1995).
- [47] P. K. Panigrahi, A. Schröder, and J. Kompenhans, PIV investigation of flow behind surface mounted permeable ribs, *Exp. Fluids* **40**, 277 (2006).
- [48] See Supplemental Material at <http://link.aps.org/supplemental/10.1103/PhysRevFluids.7.033702> for multimedia associated with Figs. 2, 3, 5, 7, 13, and 14.